NUMERICAL SIMULATION OF MECHANICAL BEHAVIOUR OF REINFORCED SHEET METALS

NUMERICAL SIMULATION OF MECHANICAL BEHAVIOUR OF REINFORCED SHEET METALS

By

BOKE, B. Eng

A Thesis

Submitted to the School of Graduate Studies

In Partial Fulfillment of the Requirements

For the Degree

Masters of Applied Science

McMaster University

Master of Applied Science
(Mechanical Engineering)

McMaster University
Hamilton, Ontario

TITLE: Numerical Simulation of Mechanical Behavior of Reinforced Sheet Metals

AUTHOR: Boke

SUPERVISORS: Dr. Allan D. Spence, Dr. Peidong Wu

NUMBER OF PAGES: xii, 100

ABSTRACT

In this study, detailed numerical analysis is carried out to investigate the effects of strain hardening on necking improvement by using finite element package ABAQUS. In addition, the response of laminated composite in necking, pure bending and hydroforming is also examined. It is concluded that the necking strain of the composite can be improved by adding high strain hardening constituent materials. Architectured structure, especially corrugated reinforcement is an efficient method to significantly improve necking strain.

When the laminated composite is under tension, the necking strain is proportional to the strain hardening rate and volume fraction of the cladding material. After unloading in pure bending process, compressive and tensile S11 residual stress exist at the top and bottom of the specimen respectively for monolithic material and soft outer layer composites. The residual stress distribution varies according to different material composition. The extent of springback is linearly related to the bending moment.

After the unloading in hydroforming process, tensile and compressive S11 residual stresses are distributed at the top and bottom surfaces of the monolithic specimen. When soft material is cladded at the outer layer of the composite, more compressive residual stress is observed in the cladding. The volume change of the specimen is linearly related to the fluid pressure while the slope of the linear function is independent to the material composition.

Under 2D plane strain tension, corrugated reinforcement is able to provide high strain hardening rate at large strain, and hence significantly improve necking strain of the composite. Small scale corrugation is superior to large scale ones in both necking strain and strength improvement. An optimal scale exists for highest necking strain and strength while further decrease of scale deteriorates the tensile response.

The anisotropic improvement of necking strain by 2D corrugation can be extended to other directions by 3D cone reinforcement. Under plane strain condition, the cone reinforcement is superior to the flat reinforcement in necking strain while remaining comparable strength.

ACKNOWLEDGEMENTS

I would like to express my sincerest gratitude to my supervisors Dr. Wu and Dr. Spence for your inspiring advice, patient instruction and motivational encouragement.

I also wish to thank Dr. Embury and Dr. Bouaziz for several valuable discussions and insightful suggestions.

Many thanks to my colleagues in research group: Xiaoxian Chen, Huamiao Wang, Jing Peng and Haoyu Li for your support and selfless help.

Special thanks to my girlfriend Xu Xin and my parents, who give me consistent love and support. Without you, I will not have this opportunity.

Many thanks also go to Novelis Inc, ArcelorMittal and McMaster University for research funding and financial support.

TABLE OF CONTENTS

LIST OF FIGURES

Chapter 1 Introduction

1.1 Composite material Overview

Composite materials, or usually called composites, consist of two or more constituent materials which have different physical or chemical properties. Unlike alloys, the constituent materials of composites are discrete and distinct. There are two major components of the composite material: matrix and reinforcement. The reinforcement is usually stronger and stiffer, and it carries the most of the load; whereas the matrix is used for keeping the reinforcement in place, assisting in bearing the load and sometimes protecting the reinforcement. In fact, composite materials have been used for thousands of years, and the earliest example of composite is mud and straw bricks. Mud is weak in both tension and compression, but is a good binding material. On the contrary, straw can withstand tensile and compressive load, however, pieces of straw cannot form certain shapes by itself. In the bricks, the straw served as reinforcement while the mud is the matrix holding the straw in place. Another common example of composite is concrete column. In the column, cement, gravel and rebar comprise the three-phase composite. The low cost cement is a good binding material and able to carry high compressive load with gravel while steel rebar is extremely strong in tension. The combination produces high tensile and compressive strength with little cost and reliability because of the corrosion protection of the steel rebar by the cement.

1.2 Types of composite

1.2.1 Particle reinforced composite

As shown in Figure 1.1, the four basic composition types are: (a) particle reinforced; (b) fiber reinforced; (c) laminated; and (d) graded composite. The above mentioned cement and gravel combination is a good example of particle reinforced composite. Another common particle composite is an automotive tire. The polyisobutylene elastomeric polymer matrix is reinforced by carbon particles that increase the modulus. When the size of the particles is small, at the order from 10^{-5} to 10^{-4} mm, it is called a dispersion strengthened composite. The fine particles hinder the slip and dislocation while the matrix carries the most of the load.

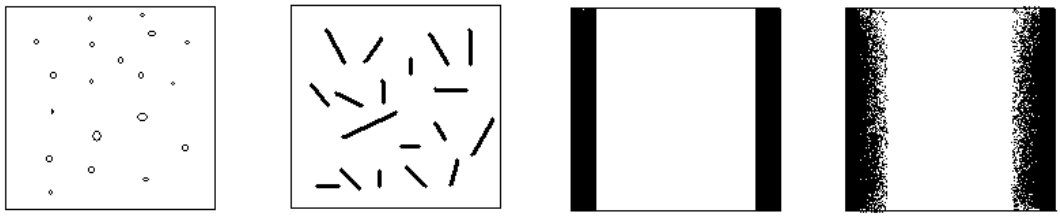

(a) (b) (c) (d)

Figure 1.1: Types of composite material. (a) Particle reinforced composite; (b) Fiber reinforced composite; (c) Laminated composite; (d) Graded composite.

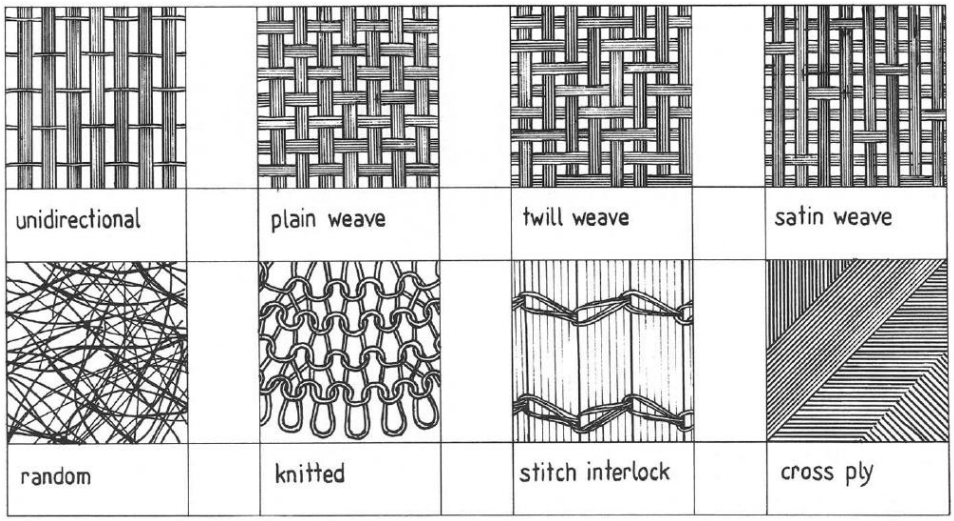

Figure 1.2: Schematic of types of fiber reinforcement [Guild et al. (1992)]

1.2.2 Fiber reinforced composite

According to different configurations of the fibers, there are many of variants of the fiber-reinforced composites. As shown in Figure 1.2, the fibers can be discrete or continuous. They can be woven to a certain pattern or just placed randomly. The most noteworthy application in this class is the carbon fiber composite. Featuring high tensile strength, low weight, low thermal expansion and high temperature tolerance properties, carbon fiber is widely used in aerospace, motorsports, military and sports equipment. Bound and protected by polymer, the carbon fiber reinforced plastic (CFRP) is famous for its high strength to weight ratio and extreme rigidity. In order to reduce weight while remain high strength in structure, Toyota decided to use CFRP to build its newly released super sports car Lexus LFA. As shown in Figure 1.3, 65% of the LFA chassis is made of

CFRP, resulting in 220 lbs of weight reduction and 0-100 km/h acceleration in just 3.5 seconds.

(a) (b)

Figure 1.3: Fiber reinforced composite example in Lexus LFA. (a) The LFA A pillar formed from carbon looming machine; (b) CFRP chassis of Lexus LFA. [http://www.clublexus.com]

1.2.3 Laminated composite

Laminate is another popular class in composite materials as shown in Figure 1.1(c). Materials with different properties are placed layer by layer and bonded by adhesives or other techniques. The combination ranges from metal with metal, metal with non-metal to non-metal with non-metal. Individual or combined improvement in formability, wear and corrosion resistance, fatigue behavior, fracture toughness and damping capacity can all be achieved in laminated composites owing to the alternating layers of different materials. For example, the body of the pot shown in Figure 1.4 is made from steel/aluminum/steel laminate. The inner and outer stainless steel layers

provide strength, wear resistance, and corrosion resistance, while the aluminum core enables fast and uniform heat distribution. As a matter of fact, mechanical behavior of laminated composites is in great interest of scholars and professionals, and as a result, much research on the subject has been reported. Chen et al. (2010) examined the improvement of ductility in sheet metal and round bar clad with ductile layer. The necking and fracture strain are increased by the ductile cladding layer. Void nucleation and void growth are delayed and the ductility is improved.

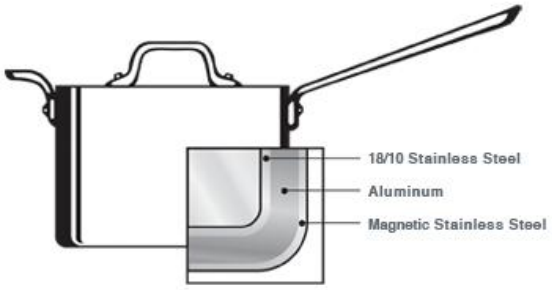

Figure 1.4: Sandwich structure of cooking ware. [http://www.hubpages.com]

1.2.4 Graded composite

Unlike the discrete interface in laminated material, the material composition and structure varies gradually from one to another in graded composites. This combines the advantages of both materials while the interface is unlikely to fail as it happens in laminated composites. A good example is the wear resistance lining in the mining industry [Ruys and Sun (2002)]. The hard ceramic face at outer side and the tough metal side at the rear are connected by a graded composition from metal to ceramic. The ceramic face can withstand intense abrasion while the rear metal end provides impact

resistance. In addition, the metallic base can be easily welded or bolted to supporting frame. Another example is the ceramic-metal graded turbine blade. The blade is exposed to extreme high temperature, reaching 1600°C. If monolithic material is used, huge variation of temperature and non-uniform thermal expansion would cause high thermal stress and the blade would crack. The gradual transition of metal and ceramic significantly reduces the stress concentration and thermal stress.

1.3 Production of composite material

1.3.1 Production of particle and fiber reinforced composite

Generally speaking, the matrix and reinforcement are combined or mixed by melting and curing events. The reinforcing particles are added into the melted matrix according to a specified volume fraction. The two constituents are carefully mixed to prevent voids and imperfection, and the solution is formed to the desired shape in moulds and solidifies. Vacuum or pressure mouldings are required in making fiber reinforced composites. The reinforcement is usually placed in the lower mould. Just enough melted matrix material is applied to stick the fibers to the desired structure. The resin is then supplied, and vacuum, pressure or autoclaves are used to wrap the reinforcement with the matrix without cavities. The process can be done in either room temperature or elevated temperature according to materials. The final shape is set by the moulds, although sometimes deformation would be used if necessary.

1.3.2 Production of laminated composite

Manufacture of metal laminated composites draws a lot of attention due to the popularity of laminate in industries. One major technique is deposition, during which material at a molecular scale is deposited and forms the lamination layer. This can be done by chemical or physical vapor deposition, sputtering, spray deposition or electroplating. Another major technique is bonding which adheres two or more solid metal plates together. According to different bonding methods, the plates can be combined by adhesion, diffusion, chemical reaction, deformation or melting [Chen et al. (2005)]. Deformation bonding, especially rolling, is widely adapted due to the low cost, easy operation and high-speed production. Roll bonding can be further categorized into two groups: hot rolling and cold rolling. Hot rolling is also known as a heat and pressure process. The plates are cleaned and heated to plastic range, and then stacked together and pressed through a pair of rolls. This process pushes the plates to seamless contact and the metal at the interface shares electrons to form the bond. Dimensional change should be taken into consideration due to the shrinkage after cooling. In cold rolling, the cleaning of the plates is very important, therefore, in most cases, both chemical and mechanical methods are applied. Then the layers of metal are combined by rolling together. The thickness reduction ranges from 50%-80%, and the plates are joined together by this large deformation. Sometimes sintering is required for accelerating the atomic diffusion. Compared with hot rolling, cold rolling features good surface quality, high strength and

better finish tolerance. However, due to the massive power demand in cold rolling, the size of the product is often limited [Davis et al. (1994)].

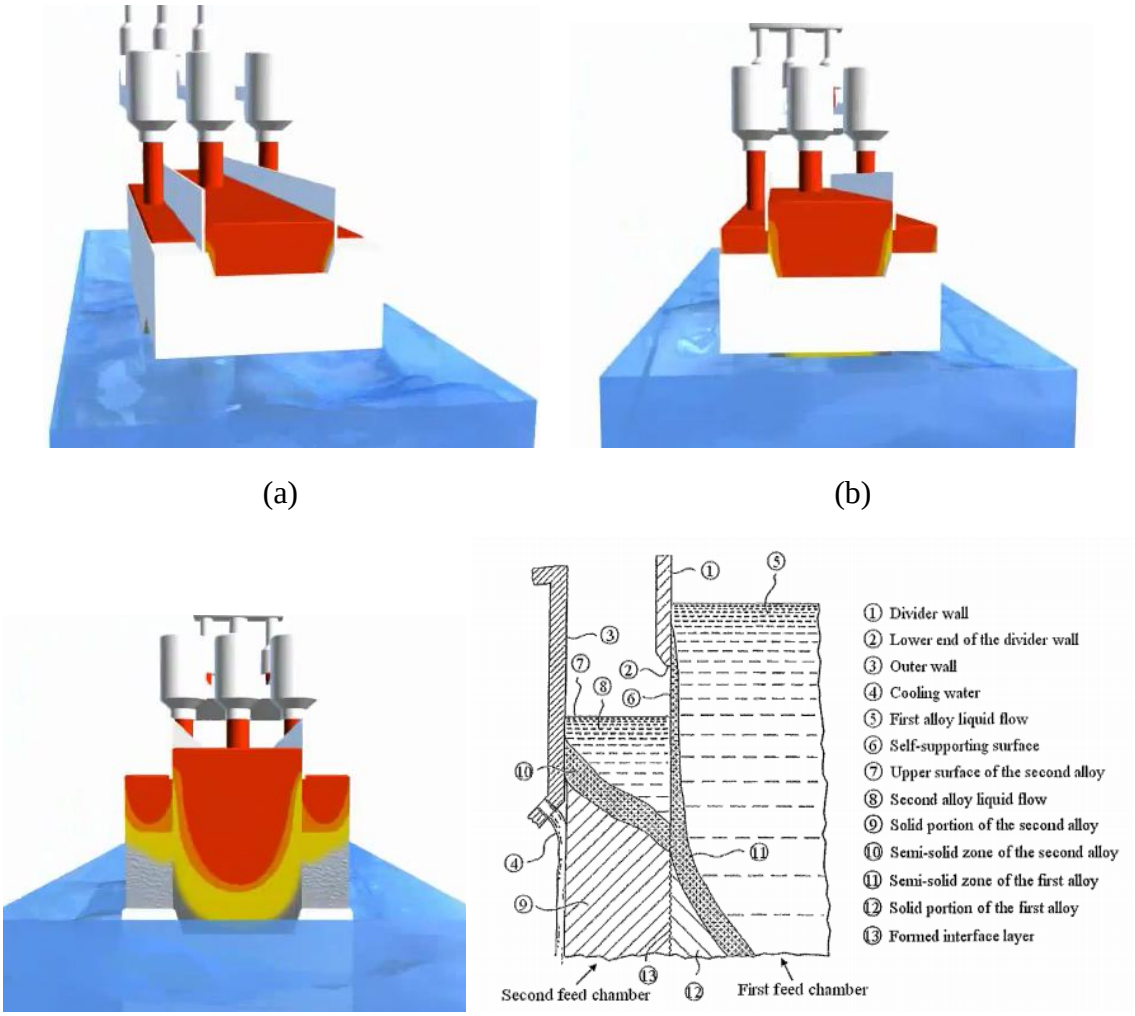

Figure 1.5: Demonstration of Novelis Fusion Technology (a), (b), and (c) Stages of Novelis Fusion Technology for casting composite ingot, (d) Schematic of Novelis Fusion Technology. [www.youtube.com, Alcan (WO 2004/112992 A3)]

Despite the effort that was made to bond the layers of metal in rolling process, defects leading to delamination are inevitable. Due to the nature of the materials, combinations that can be used to produce cladded composite are restricted. Novelis developed a new processing technique: the "Novelis Fusion Technology" which is able to solve the above problems. As shown in Figure 1.5(a), the apparatus used for casting a sandwich composite ingot includes a mould at the bottom and two divider walls. The liquid core material is filled between the two dividers and cooled by the low temperature mould at the bottom. A semi solid state is generated along the lower divider walls and mould, and a self-supporting surface is formed. After the liquid cladding material is fed into the outer chambers without contacting the core material, the mould is lowered into cooling water as demonstrated in Figure 1.5(b). Liquid cladding material starts to contact the self-supporting surface of core material, and the intimate bond is established while the two materials are solidified as the temperature is further reduced by the cooling water as shown in Figure 1.5(c). The mould is continuously lowered into the cooling water, and the liquid flow rate is maintained at the top simultaneously. By repeating this configuration, multi layers composite can be cast as well. With the help of this new "Novelis Fusion Technology", the bond between layers can be very strong and defects can be eliminated. As shown in Figure 1.6, there are no defects at the interface of AA1200 and AA2124 alloy. Figure 1.6(b) demonstrated the fracture occurs at the low strength AA1200 alloy while the interface marked is intact. Other advantages of "Novelis Fusion Technology" include: (i) conventional labor-intensive cladding process can be

simplified and the composite can be directly produced at casting stage; (ii) combination of materials for lamination is broadened.

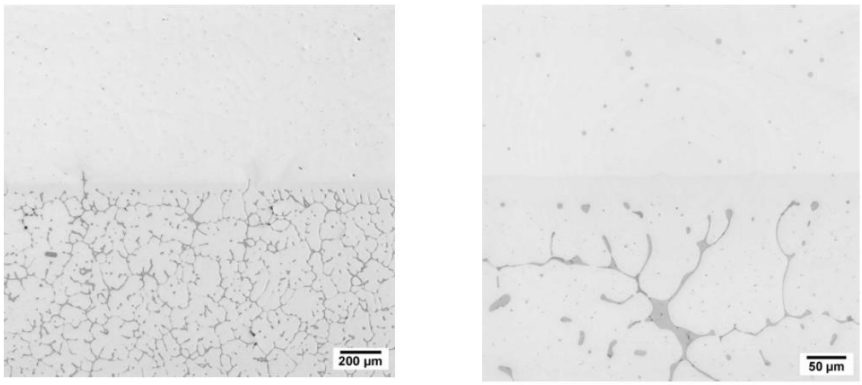

(a)

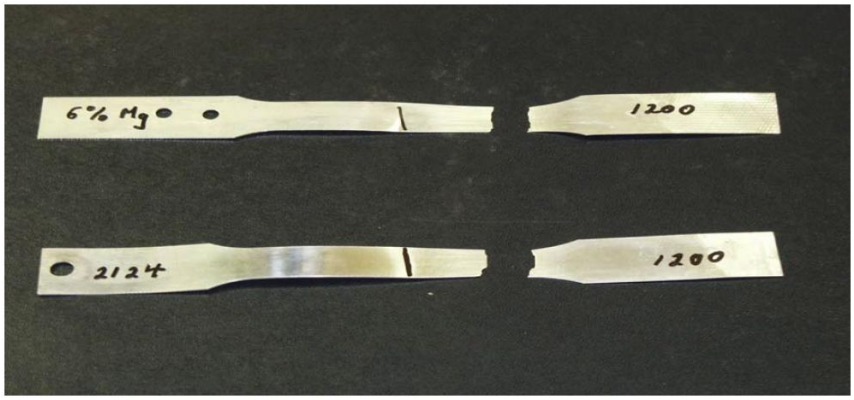

(b)

Figure 1.6: Evidence of strong bonding produced by Novelis Fusion. (a) Microstructure of inAA1200/AA2124 interface; (b) Fracture at low strength alloy in tensile test. [Wagstaff et al. (2006)]

1.3.3 Production of graded steel

Having many available simple methods to alter microstructure feature makes steel a good candidate to manufacture graded composites. Tempering, annealing, recrystallization, controlled duration for phase transformation, heavy deformation or even

temperature can change the microstructure and mechanical properties. Another traditional way to produce graded steel based composite is diffusion, such as carburizing or decarburizing and nitriding. Decarburizing heat treatment will be used as an example because of its fast and economic features. Removing carbon from the specimen surface while prevent the steel from being oxidized is the goal of decarburization. The decarburizing gas needs to be able to both react with and release oxygen, so the carbon in steel can be extracted by oxygen while the excessive oxygen can be controlled and not oxidize the specimen surface. H_2/H_2o is a good decarburization mixture. A subtle pressure of oxygen in the mixture is maintained so there is not enough oxygen to react with steel, but it can combine with carbon at the surface and extract it. Another approach is by using CO/CO_2 mixture. The ratio of CO and CO_2 can be changed to any value to cause decarburization or carburization. With the presence of carbon in the mixture, any desired value of carbon concentration at the steel surface can be achieved. On the contrary, carbon concentration at the surface can only be set to zero when using H_2/H_2O mixture. Besides the carbon content at the surface, the depth or the volume fraction of the decarburization zone can be controlled by the heat treatment duration [Bechir et al. (2009)].

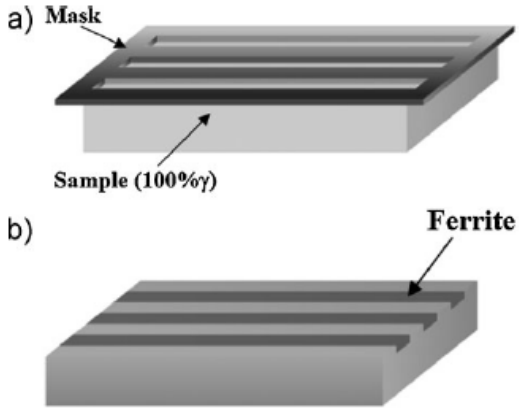

Figure 1.7: "Extrinsic mask" technique. [Bechir et al. 2009]

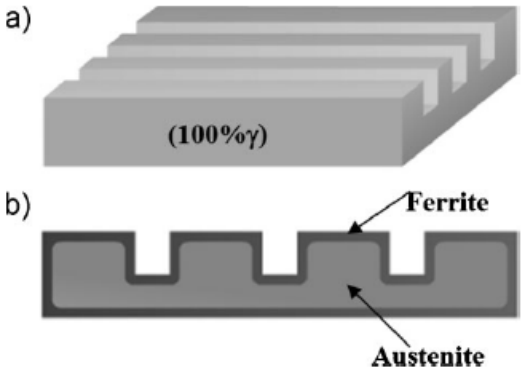

Figure 1.8: "Intrinsic mask" technique. [Bechir et al. 2009]

Simple decarburization techniques will produce coaxial or sandwich graded composite which are limited in application. More complex patterns can be made by masking methods based on simple rod, tube or plate specimen. The idea is to partially decarburize the specimen and create certain feature. The base sample can be covered by an "extrinsic" copper mask with specific features, so parts of the sample can be decarburized and the microstructure under the mask remains unchanged as shown in Figure 1.7. However, the base materials are easily damaged when the mask is applied or removed. The procedure is costly and labour-intensive. Another "intrinsic" mask technique can be implemented to solve the above difficulties. As shown in Figure 1.8(a), the base sample is grooved by machining and then followed by uniform decarburization. The excessive grooves can be removed by machining, and a combination of decarburized and non-decarburized surfaces is generated [Bechir et al. (2009)].

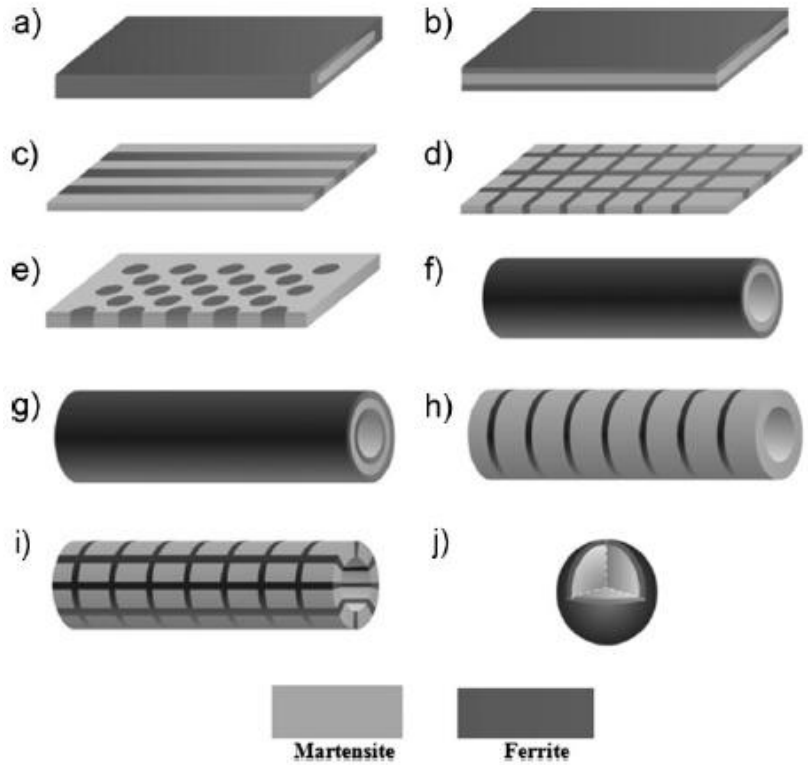

Figure 1.9: Possible patterns created by partial decarburization. [Bechir et al. (2009)]

Decarburization of hard martensite produces soft and ductile ferrite. With the masking technique, series of graded steel composite can be manufactured as illustrated in Figure 1.9, and various beneficial properties can be obtained. For example, the ductile outer layer of Figure 1.9(a) can improve the formability. With one direction distribution of ferrite, Figure 1.9(c) possesses un-isotropic property of high strength in one direction while high formability in the other. Various patterns of graded steel composite will provide many potential applications and attract significant researcher attention.

1.4 Literature review of techniques for improving necking strain and formability.

According to Considere's theory, necking occurs at the strain where the true stress strain curve and strain hardening rate curve intersect. As shown in Figure 1.10, to delay necking, in other words, delay the intersection of the two curves, either the stress curve should be shifted down or the strain hardening curve should be shifted up. Lowering the stress will compromise the strength of the material and fail to meet load carrying requirement. Therefore, increasing strain hardening rate while at the same time keeping the stress state, can delay necking and hence improve formability without compromising the material strength. This field has been of special interest to numerous researchers in material science and mechanical engineering. Metallurgical processing, laminated materials [Chen et al. (2010); Chen et al. (2010)(2)], compositionally graded materials [Bouaziz et al. (2008)], architectured materials [Embury et al. (2010)], Twinning Induced Plasticity [Mirko et al. (2003); Bouaziz et al. (2001); Bouwhuis et al. (2010)] and Transformation Induced Plasticity [Dan et al. (2007); Yan et al. (2007)] have been employed in solving this problem.

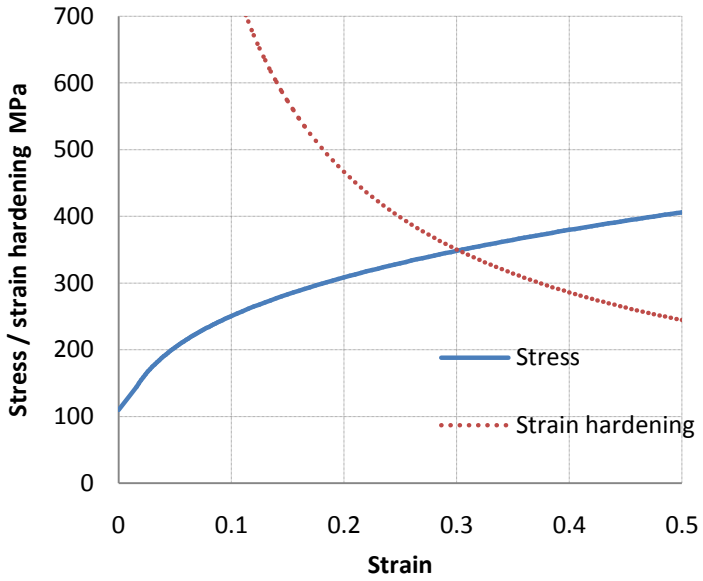

Figure 1.10: Stress/strain hardening rate versus strain curves for typical power law hardening material.

The work hardening rate can be improved by altering microstructures of metals. Microfeatures such as second phase partical, disperstion or deformation twins can phasically affect meterial's deformation mechanism. Song et al. performed various experiments showing that increasing volume fraction of finely dispersed cementite particales can improve strain hardening rate of ultrafine grained steel. Although grain refinement reduces ductility, the increase of work hardening is large enough to overcome the negative effect. In austentic steels, deformation twins impede the gliding of dislocations and therefore increase the work hardening and strength. A formulation describing the interaction between the twins and gliding dislocations is examined in [Bouaziz et al. (2001)]. The TWIP steel is also used in microtruss cells as a strengthening mechanism [Bouwhuis et al. (2010)]. In other cases, the austenite transformed to

martensite under deformation. Despite the initial softening caused by volume expansion, the work hardening rate and strength are improved by the austenite martensite phase transformation. The effect of this transformation is examined and modeled in [Dan et al. (2007); Yan et al. (2007)]. Chen et al. (2010) investigated the necking strain and fracture strain improvement of a metal sheet by cladding high work hardening mateiral. The high strength core and low strength high work hardening cladding composite experiences plane strain tensile stretch up to fracture, which is simulated by FEA. The average strain hardening rate and necking strain are increased by the cladding material while the strength is slightly decreased. The delayed necking reduces the triacial tensile stress in the neck and impeded the void nucleation and coalesence. In turn, the fracture strain is improved as well. The similar mechanics is applied in round tensile bars, and promising results are observed [Chen et al. (2010) (2)]. Instead of lamination, ductile layers can be added to composites by graded material to increase work hardening. Bechir et al. (2009) proposed the outer surface of a martensitic block can be transferred to ductile ferrite by decarburization, so the overall necking strain can be improved. Bouaziz et al. introduced a new architectured material which efficiently improves strain hardening rate by embedding corrugated reinforcement in steel matrix [Bouaziz et al. (2009)]. The independent corrugation strip is made by compressing a flat steel strip between two anvils. The corrugation geometry can be changed by different roller size and spacing. In uniaxial tensile process, the corrugations bring additional elongation to enhance the necking strain. Combined with matrix material, the work hardening at high strain is improved significantly by the straightening of the corrugated reinforcement. The effect is

qualitatively studied by FEA using perfect plastic materials for both matrix and reinforcement. Figure 1.11, is the strain hardening rate versus strain curve for corrugation reinforced composites. The strain hardening rate increases as the composite is strained and it peaks at 0.22 strain for h/p=0.28 case. In contrary, the strain hardening rate for straight reinforced composite is zero due to the properties of perfect plastic materials. The strain hardening rate for h/p=0.5 case increases with the strain as well, but it peaks at larger strain.

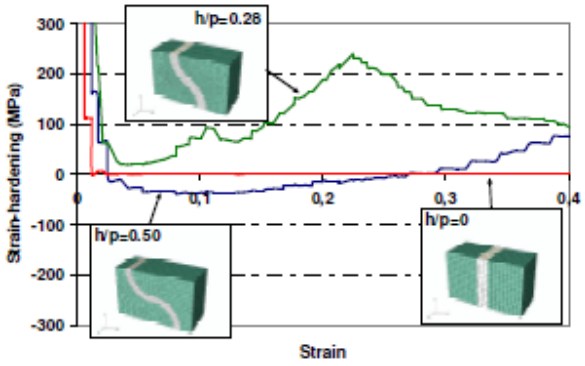

Figure 1.11: Strain hardening rate for corrugation reinforced composites. [Bouaziz et al. (2010)]

Formability has two major aspects, which are deep drawability and stretchability [Paul et al. (1996)]. Drawability represents the ability of material to resist reduction of thickness while it can easily flow in the sheet plane directions. Drawability is proportional with plastic strain ratio [Whiteley et al. (1961)]. On the other hand, stretchability measures how well the material can resist localized necking, and it is directly related to the work hardening rate. The higher the work hardening rate, the better the material can distribute strain uniformly, resulting higher formability for steels [Keeler and Brazier

(1977)]. Kang et al. (2009) also suggested that stretch formability is linearly related to work hardening rate for magnesium alloys.

Yoshida examined that plastic deformation induces rotation of grains, and this rotation changes crystallographic textrue and strength of the material. This phenomenon is a new class of work hardening called geometrical or texture hardening which can be controled to significantly enhance formability [Yoshida et al. (2009)]. One thing should be pointed out that work hardening rate is a good measure of formability in mateirals with same base elements. It can not be used to compare formability between different materials. Kleemola and Kumpulainen have discovered that the formability of steel is higher than aluminum, although steel has lower work hardening rate than aluminium. The reason is that the work hardening rate and anisotropy value of aluminium start to decrease at large strain, especially in plane strain condition. Likewise, Shapiro et al. (1983) have found that formability for high strain hardening rate copper and brass is lower than mild steel which has low strain hardening.

1.5 Literature review of spring back and residual stress study for purebending and hydroforming

Stress occurs when the material is strained. Within the elastic deformation range, the stress completely disappears after external load is removed. However, under plastic deformation such as metal cutting and metal forming or heat treatment, sometimes a

residual stress remains even after the external load is removed. Residual stress may cause failure to cast component while it can be beneficial when under control. Compressive residual stress can improve fatigue behavior, corrosion resistance and fracture toughness. For example, compressive residual stress is introduced to automotive transmission gears and shafts by shot peening to extend fatigue life.

After bending process, the residual stress and elastic unloading of stressed material cause the specimen to unbend. This phenomenon is spring back. Spring back is related to the material, type of bending and the degree of bending. Spring back causes the reduction of bend angle and change of finishing geometry, so it has to be taken account for dimensional accuracy.

Residual stress distribution and spring back of bending process is widely investigated due to its significance in manufacturing process and load capacity calculation of bending part. Research activities range from pure bending [Perduijn et al. (1993)] to stretch bending [El-Megharbel et al. (1990)], small curvature bending to large curvature bending [Zhu et al. (2006)], analytical method to numerical method and two dimensional modeling to three dimensional modeling. [Zhang et al. (1998)] has investigated the residual stress - spring back relation in plane strain bending. Possible causes of discrepency between earlier researches have been documented.

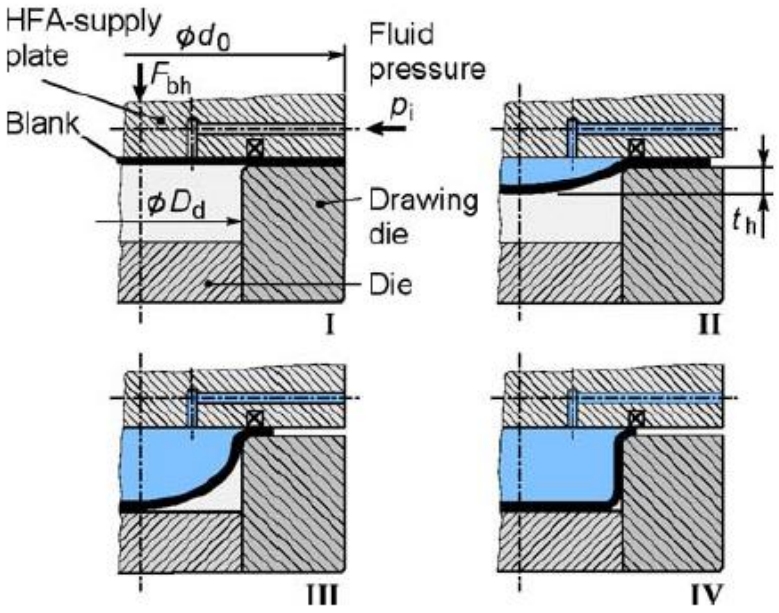

Figure 1.12: Schematics of hydroforming process. [Kleiner et al. (2004)]

Hydroforming, also known as high pressure sheet metal forming, is a sheet metal forming process used to manufacture complex geometry parts. It is widely adapted in automotive industry. For instance, vehicle body components, suspension, radiator supports and engine cradles are all manufactured by hydroforming. As demonstrated in Figure 1.12, the metal sheet is clamped between blank holder and drawing die. A cavity with desired shape is formed between the drawing die and die. High pressure fluid is then pumped between the sheet and blank holder, and the sheet is deformed until it is against the die. The process involves bending or sometimes unbending, therefore spring back and residual stress causes change of final dimensions. [Kleiner et al. (2004); Bruni et al. (2007)] and other researchers conducted investigations about spring back and residual stress in hydroforming.

1.6 Thesis outline

In composite materials, failure is most likely occur at the interface between different constituents. For instance, delamination is the most common failure mode in laminated composites. Fortunately, Novelis Fusion Technology and compositionally graded material are able to produce a strong interface that won't trigger failure of the composite. Based on this strong interface, finite element models are developed to examine necking behavior, spring back and residual stress distribution in pure bending, and spring back and residual stress distribution in hydroforming for laminated composites. Numerical study and finite element analysis are conducted in investigating the strain hardening rate and formability improvement by corrugated reinforcement.

Chapter 2 presents the numerical simulation and analysis for effects of clad and core material properties on necking for laminated material. Then, spring back and residual stress distribution for pure bending and hydroforming for laminated material are investigated by finite element simulation. Chapter 3 is dedicated to the work done in numerical study and analysis of the work hardening and necking strain improvement induced by corrugated reinforcement in 2D finite element models. Chapter 4 demonstrates investigation of strain hardening rate and formability improvement by corrugated reinforcement in 3D finite element models.

Chapter 2 Response of laminated composite in necking, pure bending and hydroforming

2-1 Parametric study of necking in laminated metal composite

2-1-1 Introduction

Necking of monolithic material sheet and bar has been extensively investigated. The onset of necking, shapes, deformation, stress, and strain distribution of tensile specimen has been studied and documented [Chen et al. (1971); Needleman et al. (1972)]. According to Considere's theory, power law hardening material necks when the strain equals the strain hardening index. Increasing the strain hardening index n is an efficient way of increasing necking strain. [Chen et al. (2010)] examined that increasing the average strain hardening rate by cladding a ductile layer can improve the overall ductility of the laminated composite sheet. Similar numerical investigation has been conducted for round tensile bars as well [Chen et al. (2010) (2)]. In this section, effect of parameters such as clad and core material strain hardening rate, clad thickness ratio and imperfection on necking of laminated sheet is studied.

2-1-2 Results and discussion

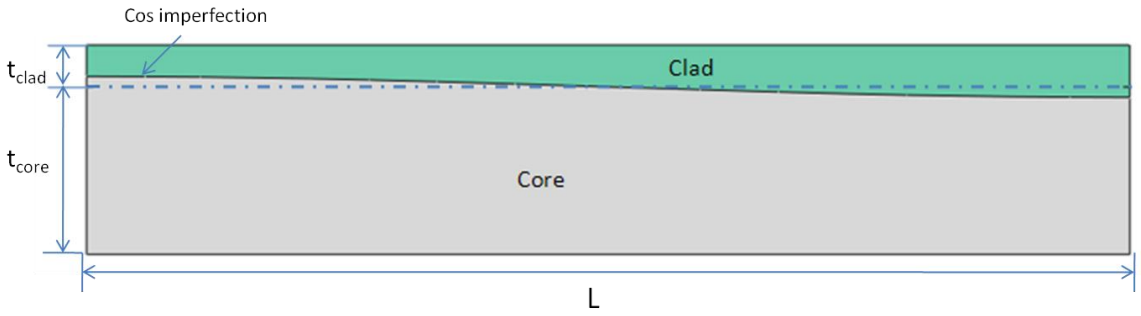

$$t_{total} = t_{clad} + t_{core} = 1 \qquad L = 5$$

Figure 2.1.1: Schematic representation of laminated composite.

As shown in Figure 2.1.1, a rectangular specimen is modeled. The length of the specimen L is 5, and the total thickness is 1. Previous research suggested that the aspect ratio L/t should be greater than 4 in order to promote accurate simulation of necking. Therefore, the length of the specimen L is specified to 5 in the research. The depth into the page is assumed to be infinite and plane strain condition will be modeled. The cladding material is added on top of the core. The interface between the clad and core is a cosine wave which has very little amplitude to trigger the onset of necking. As mathematically described in (2-1-1), the amplitude δ is 0.0008, and the wave number A is 1 for initial cases.

Cosine wave imperfection:

$$\delta \cos(A\frac{x\pi}{L}) \tag{2-1-1}$$

Material behavior:

$$\sigma = K\varepsilon^{n} \tag{2-1-2}$$

The left side and bottom side of the specimen is constraint in x direction and y direction respectively to ensure symmetric condition about the left side and bottom side. X direction displacement is applied to the right side to pull the specimen until necking occurs. The material obeys a power hardening law as described in (2-2-2). The core material has yield stress σ_{y1} of 120 MPa, strength coefficient K_1=300 MPa and work hardening rate n_1 of 0.02. On the other hand, the clad material has following properties: σ_{y2}=43 MPa, K_2=183 MPa and n_2=0.2. The properties are chosen in suitable range and used for parametric study of how necking can be triggered and affected.

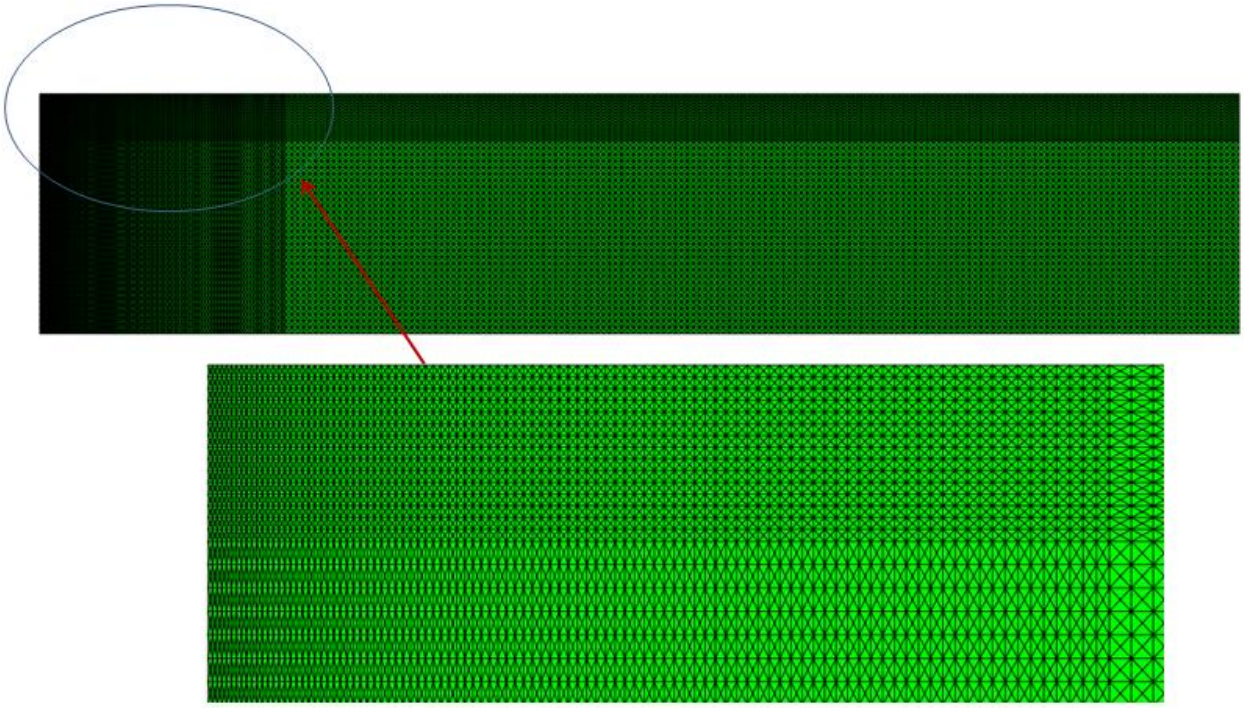

Figure 2.1.2: CPE3 Mesh.

To ensure the accuracy and reduce computation, triangular CPE3 elements which are arranged to construct rectangular units are used as shown in Figure 2.1.2. This mesh

configuration is previously employed by Wu [Wu et al. (2004)], and proved to be efficient in mapping various material properties to one single element [Inal et al. (2008)]. The mesh in the area close to the left side is more refined than the rest of the model. Even in this refined region, the mesh dimension along x direction is biased to compensate the large deformation in localized necking. More elements per unit distance along Y direction in cladding material are also implemented to accommodate the composite structure. After series mesh sensitivity studies, 40,000 to 50,000 elements are proved to have convergent results and will be used in subsequent analysis.

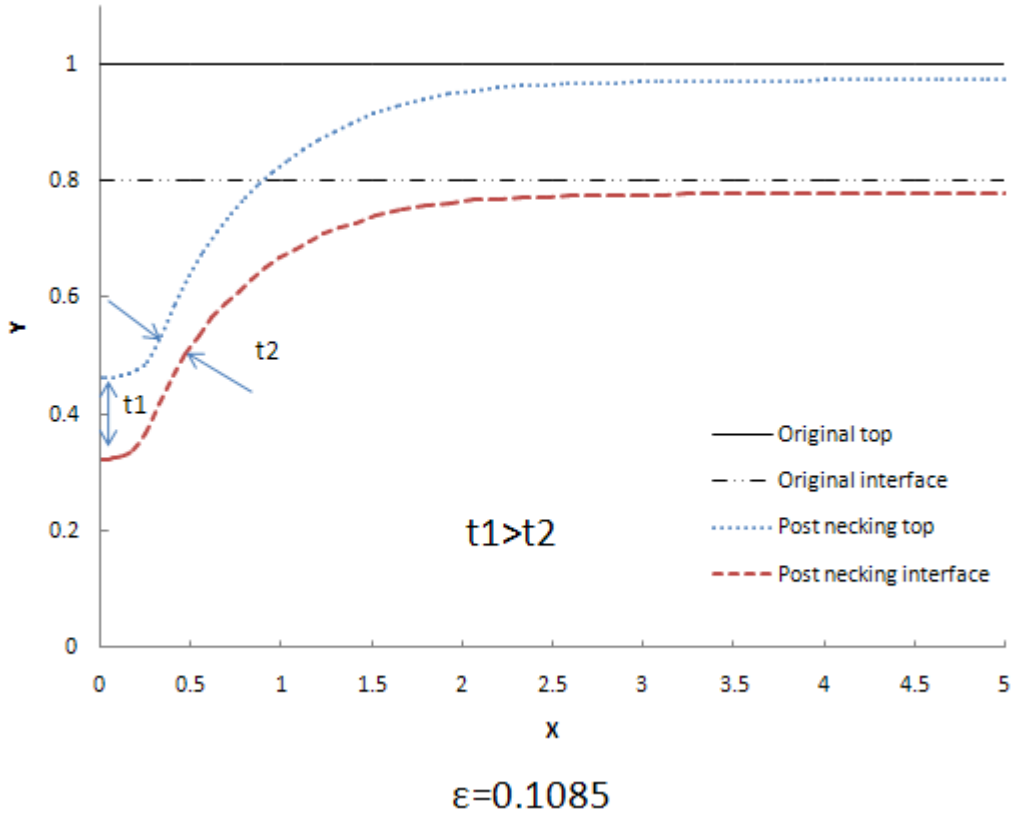

Figure 2.1.3: Profiles of top surface and interface.

Figure 2.1.3 is the profile of the top surface and interface at original state and post necking state. The original total thickness is 1 and the thickness of cladding is 0.2. At strain of 0.1085, localized necking is well developed. The minimum total thickness at the left side is 0.464, and the minimum core thickness is 0.323. Interestingly, the minimum thickness of core is at the left side while the minimum thickness of clad is somewhere around 0.4 from the left side. At the section far from necking area, the thickness of the composite and core are 0.974 and 0.78 respectively, leaving the thickness of the cladding 0.194.

Recalling the cosine wave imperfection equation (2-1-1) $\delta \cos\left(A\frac{x\pi}{L}\right)$, the imperfection amplitude effect on necking is examined by first changing the magnitude of the amplitude. As shown in Figure 2.1.4(a), the amplitude is changed from 0.0008 to 0.001 to 0.0012 with single wave. The tensile behaviors are identical for the three cases. The number of cosine waves is then changed from 1 to 5 and to 9 with constant amplitude of 0.0008. As shown in Figure 2.1.4(b), the wave number barely affects the reaction force and necking of the laminated composite. Therefore, the imperfection has no influence on tensile behavior, and single cosine wave with amplitude of 0.0008 will be used in subsequent analysis.

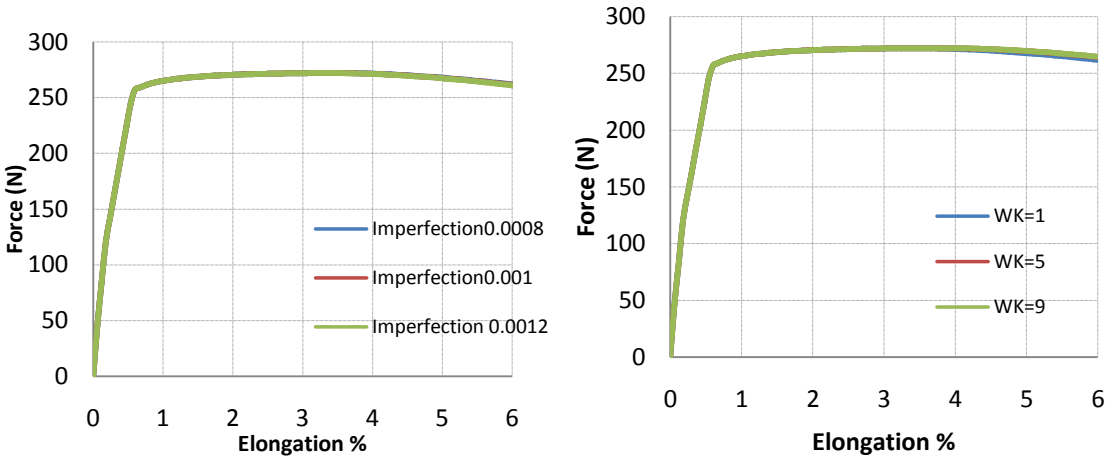

(a) (b)

Figure 2.1.4: Reaction force vs. Elongation % for (a) Different imperfection amplitude, and (b) Different imperfection wave number.

According to Considere's theory, necking occurs when the following expression is satisfied.

$$\sigma = \frac{d\sigma}{d\varepsilon} \tag{2-1-3}$$

Assuming both core and clad material obey power hardening law and the volume fraction for the cladding material is ρ. The stress and strain relation for the laminated composite can be expressed as:

$$\sigma = (1-\rho)k_1\varepsilon^{n_1} + \rho k_2\varepsilon^{n_2} \tag{2-1-4}$$

Taking derivative of both sides:

$$\frac{d\sigma}{d\varepsilon} = n_1(1-\rho)k_1\varepsilon^{n_1-1} + n_2\rho k_2\varepsilon^{n_2-1} \tag{2-1-5}$$

When the stress equals to the strain hardening rate:

$$(1-\rho)k_1\varepsilon^{n_1} + \rho k_2\varepsilon^{n_2} = n_1(1-\rho)k_1\varepsilon^{n_1-1} + n_2\rho k_2\varepsilon^{n_2-1} \quad (2\text{-}1\text{-}6)$$

$$\varepsilon = \frac{\rho(n_2k_2\varepsilon^{n2} - n_1k_1\varepsilon^{n1}) + n_1k_1\varepsilon^{n1}}{\rho(k_2\varepsilon^{n2} - k_1\varepsilon^{n1}) + k_1\varepsilon^{n1}} \quad (2\text{-}1\text{-}7)$$

ρ: volume fraction of cladding material.

k_1 : strength coefficient of core.

k_2 : strength coefficient of clad.

n_1 : work hardening index of core.

n_2 : work hardening index of clad.

According to equation (2-1-7), necking strain can be predicted by material properties such as k_1, k_2, n_1, n_2 and ρ. Firstly, the effect of volume fraction on necking is examined by keeping constant k_1, k_2, n_1, n_2 while ρ is changed from 0 to 1. The same materials mentioned earlier are used. σ_{y1}=120 MPa, k_1=300 MPa, n_1 = 0.02, σ_{y2}=43 MPa, K_2=183 MPa and n_2=0.2.

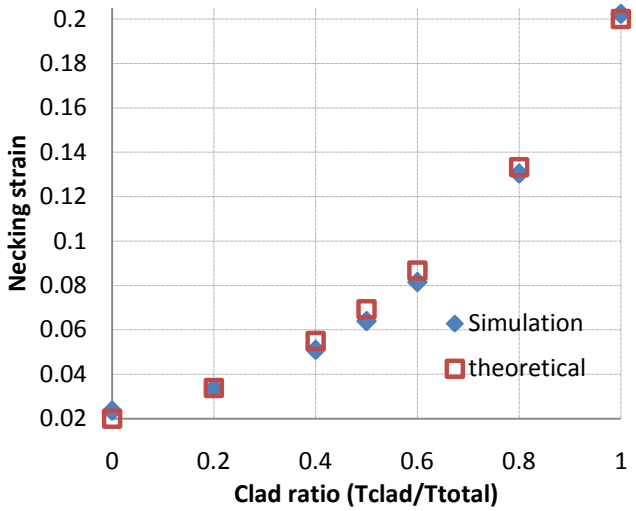

Figure 2.1.5: Clad ratio effect on necking strain.

The core material is stronger but tends to neck earlier comparing with the clad material. Necking strain of the laminated composite is plotted against the clad ratio in Figure 2.1.5. Due to the plane strain assumption, the depth into the page is infinite, and the volume fraction of the clad is equal to the ratio of the clad thickness and the total thickness. According to Figure 2.1.5, the necking strains predicted by equation (2-1-7) match the simulation results well. When the clad ratio is 0, the whole specimen is made of core material and the necking strain is 0.02 which is the hardening index of the core material n_1. As more clad material is added to the composite, the necking strain increases. When the clad ratio is 1, the case is pure clad sheet under tensile test. The necking strain equals the hardening index of clad n_2=0.2. Interestingly, the relation between the necking strain and the clad ratio is not linear. The slop tends to increase as the clad ratio grows.

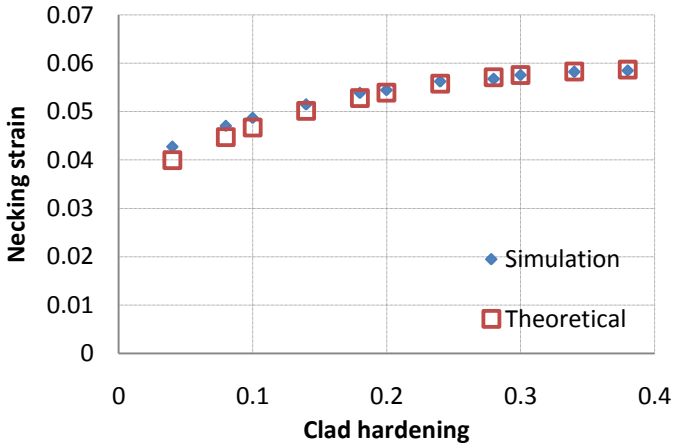

Figure2.1.6: Clad hardening effect on necking strain.

Moreover, clad material hardening effect on composite necking strain is studied. The clad hardening index is increased from 0.04 to 0.38 while other properties are kept constant, for example, σ_{y1}=120 MPa, k_1=300 MPa, n_1 = 0.04, σ_{y2}=43 MPa, K_2=183 MPa and clad ratio ρ=0.2. The results from simulation and equation (2-1-7) are plotted and compared in Figure 2.1.6. According to Figure 2.1.6, simulation and theoretical results match each other well with little discrepancy in low n_2 cases. When both clad and core material hardening index are 0.04, the composite necks at strain of 0.04. As n_2 is gradually increased to 0.38, the necking of the composite is delayed to 0.0585. Therefore, high clad hardening index is associated with high necking strain of the composite. The slope tends to decrease as the n_2 increases.

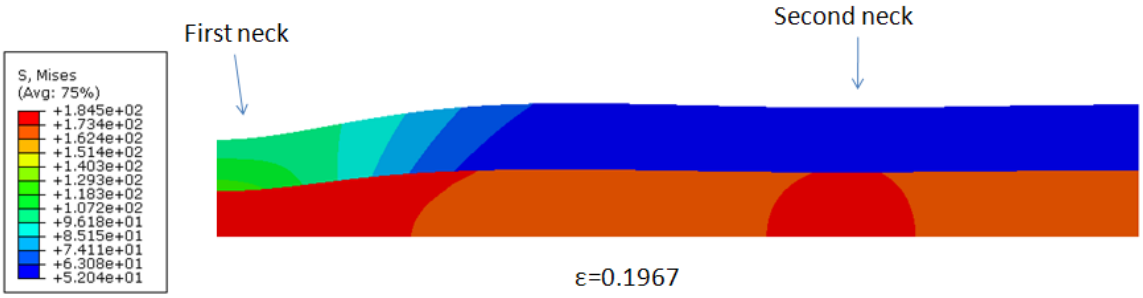

Figure 2.1.7: Demonstration of multiple necking.

Another interesting phenomenon in tensile test is multiple necking as illustrated in Figure 2.1.7. In this case, the yield stress of core and clad are σ_{y1}=120 MPa and σ_{y2}=43 MPa respectively. Strength coefficient k_1 is reduced to 188 MPa which is slightly higher than k_2 of 183 MPa. The hardening of core n_1 = 0.04 while n_2 is dramatically increased to 0.65. The half of the composite is made of clad material. Usually after instability, the thickness is reduced at one location and the stress at the rest part of the specimen is reduced due to plastic unloading. The necking is localized at that location and the thickness is continuous shrinking. In some cases, especially when the work hardening rate is very high, the material in the neck experiences a rapid increase of stress. The reduced cross section area can be compensated by the high stress state at the neck, resulting in a second neck occurring at less work hardened area. Multiple-necking phenomenon happens with certain combination of core and clad materials, and it will disappear with increase of clad material hardening.

2-1-3 Conclusion

Increasing clad material thickness ratio improves the overall strain hardening and necking strain. However, the relation between the clad thickness ratio and the necking strain is not linear. The effect tends to be more pronounced at high ratio. The cladding material hardening index has positive effect on necking strain. The equation (2-1-7) derived from mixture equation (2-1-4) can be a good prediction of necking for laminated composite.

2-2 Spring back and residual stress distribution of pure bending and hydroforming

2-2-1. Introduction

After a large plastic deformation, residual stresses may be left in the material. This locked-in stress has great influence on mechanical behavior of the material. Tensile residual stress may deteriorate fatigue life, promote corrosion or decrease fracture toughness whereas compressive residual stress does the opposite. Therefore, residual stress attracts significant attention in the manufacturing industry.

Pure bending is a condition in which the specimen is under pure moment. Without axial, shear or torsional stresses, analysis of model under pure bending is direct and many analytical relations are derived. After the bending process, the bend angle shrinks due to the elastic nature of the material. This shrinkage of bend angle is spring back. Much research has been conducted on spring back due to its importance in residual stress and final geometry of the parts.

The hydroforming process is used for producing parts with complex geometry, especially in automotive industry. As illustrated in Figure 1.12, the part is deformed by the high pressure liquid or gas between the top plate and the blank, and the shape is controlled by the dies. Since sheet metal experiences bending and unbending in hydroforming, spring back and residual stress play an important role. The spring back and residual stress investigation in both pure bending and hydroforming of monolithic metal sheet are widely conducted. However, little has been done for composite materials. In this

chapter, spring back and residual stress distribution of laminated composite is investigated.

2-2-2 Pure Bending

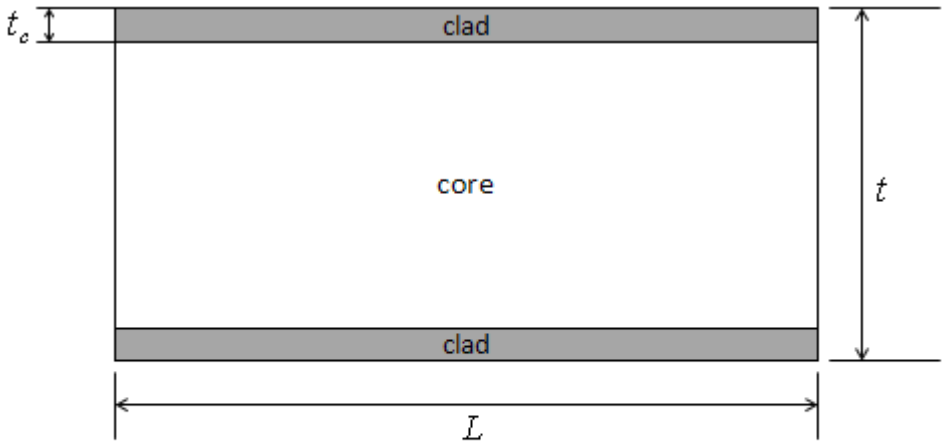

Figure 2.2.1: Schematic of sandwich composite.

A segment of the composite sheet under pure bending is modeled as in Figure 2.2.1. The length of the segment is 2mm, and the total thickness is 1mm. The cladding material can be placed at the top and bottom surface with the thickness of 0.1mm, which gives the volume fraction of 20%. The structure of the composite can be changed by different combinations of the cladding and core materials such as cladding at the top only, cladding at the bottom only, or cladding at various locations inside the core. In this section, the cladding material is limited to the outer surface because of the advantages of

cladding material in corrosion resistance and improvement of bendability, which can be efficiently implemented. Both the cladding and core materials are isotropic strain hardening material featuring yield stress 43 MPa, strain hardening index n=0.204, strength coefficient K= 183 MPa and yield stress 110 MPa, n=0.3, K=500 MPa respectively. They all have the same Young's modulus 70 GPa and Poisson's ratio 0.3. The left edge is constrained in horizontal direction while the right edge is bent to 60 degrees by MPC to ensure pure bending condition, in which the total force at the ends equals zero. The MPC is then eliminated, and spring-back and residual stress are analyzed.

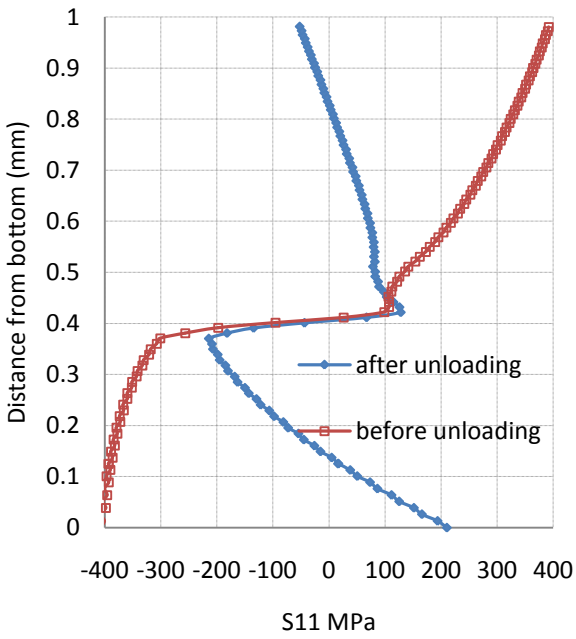

Figure 2.2.2: Pure core material S11 residual stress.

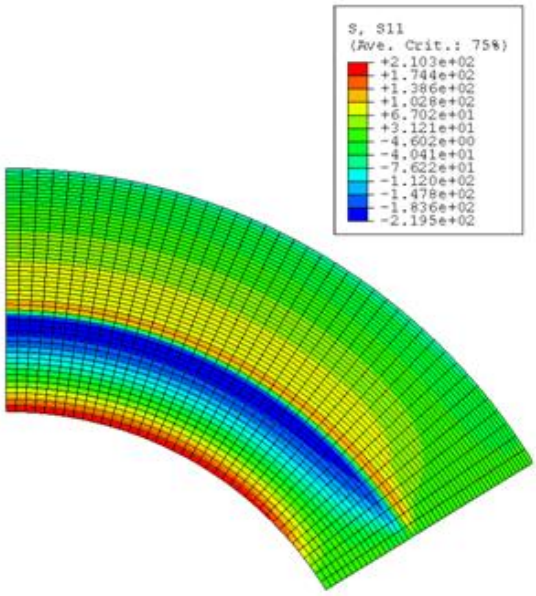

Figure 2.2.3: S11 contour after unloading for pure core case.

As shown in Figure 2.2.2, the x direction stress along the left edge is recorded at the end of bending and after the unloading for sheet with pure core material. Before unloading, the neutral axis shifted down from the geometry center. This phenomenon will be discussed later on. During the bending process, the thickness reduced by only 2%, therefore, using the true distance from the bottom is acceptable. The top half of the sheet experiences tensile stress while the bottom half experiences compressive stress and the magnitude increases as the location far away from the neutral axis. The rapid change of slope indicates the occurrence of yielding. After unloading, the stress moves to the opposite direction. For the section above the neutral axis, the tensile stress magnitude reduces, and at the area near the surface, the stress even goes to compressive and vice versa. The location which is distant from the neutral axis experiences higher plastic strain, while the central area is still within the elastic range. The fraction of the recovered plastic strain during unloading over the total strain is smaller for larger plastic deformation than it is for small plastic deformation. In addition, the cross sections that are perpendicular to the page remain in planes all the time. Therefore, while keeping the right edge straight, the shrinkage caused by the recovered strain at central area is larger than the shrinkage caused by unloading of the material at the top surface. The straight right edge tends to compress the top surface while the top surface shows resistance, which is the reason for compressive residual stress at the top surface. This mechanism applies to the bottom portion, and induces tensile residual stress at the bottom surface.

An interesting trend is noticed that at the end of bending, the slope change of the curve in Figure 2.2.2 is 100 MPa above neutral and -300 MPa below the neutral axis. In other words, the material starts to yield when S11 equals 100 MPa in the top half, but -300 MPa at the bottom. This asymmetry reduces but still exists after unloading. Keeping in mind that the isotropic hardening material is used, this phenomenon is unusual. Remaining stress components through the thickness are examined more closely below.

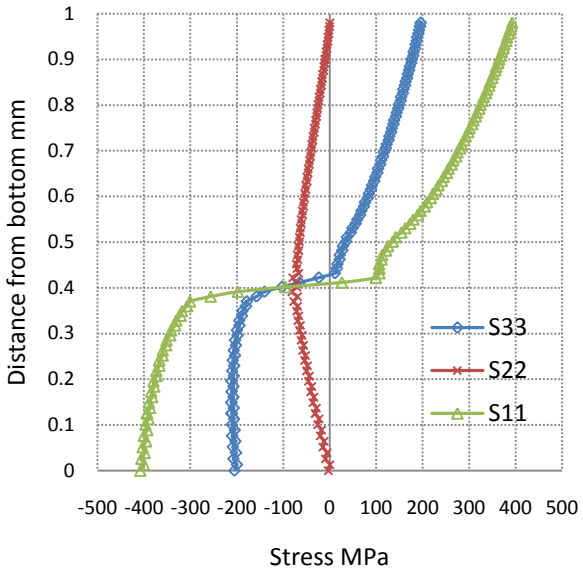

Figure 2.2.4: Stress distribution for pure core case along left edge.

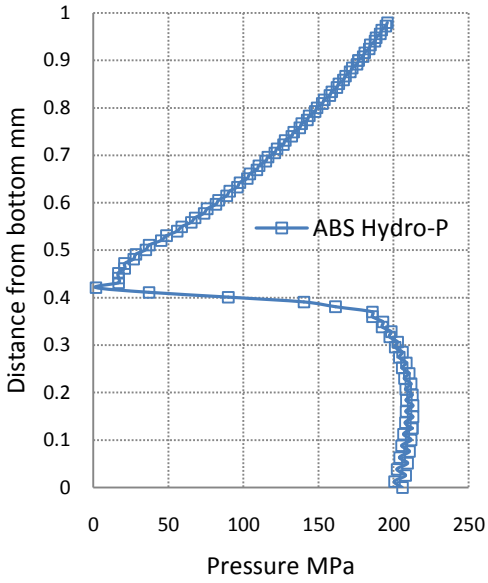

Figure 2.2.5: Absolute hydrostatic pressure distribution for pure core case.

Figure 2.2.4 shows the stress distribution for length direction S11, thickness direction S22 and in page direction S33 along the left edge of the sheet at the end of bending. S33 has similar trend as S11 but with smaller magnitude. Due to the fact that the sheet is thinned after bending, the S22 is compressive through the thickness with maximum magnitude occurs at the neutral axis and zero at the top and bottom free

surfaces. According to Mises yield criteria, yielding is independent of the hydrostatic pressure. The compressive S22 stress neutralizes the tensile S11 and S33, and thus, results in low hydrostatic pressure above neutral axis. The deviatoric stress reaches yielding point of 183 MPa when the value of S11 component is only around 100 MPa. On the contrary, all three stress states are negative below the neutral axis, inducing high magnitude compressive hydrostatic pressure. Less portion of the S11 is contributed to the deviatoric stress, which causes material yielding when S11 is -300 MPa below the neutral axis. Figure 2.2.5 is the absolute hydrostatic pressure distribution along the left edge. As predicted, the hydrostatic pressure slowly increases from 0 at the neutral axis to 200 MPa at the top surface for the top half while it rapidly changes to around 200 MPa right below the neutral axis and remains to the bottom surface.

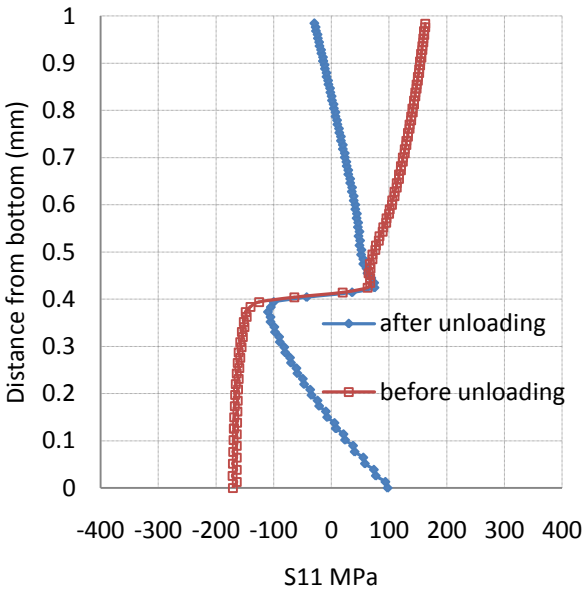

Figure 2.2.6: Pure clad material S11 residual stress.

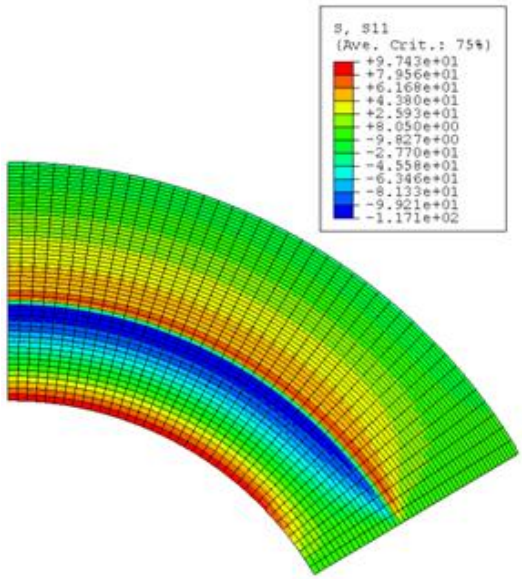

Figure 2.2.7: S11 contour after unloading for pure clad case.

Figure 2.2.6 is the S11 distribution along the left edge for pure cladding material before and after unloading. The trends are similar to the pure core case except for smaller stress value due to the softer nature of the cladding material.

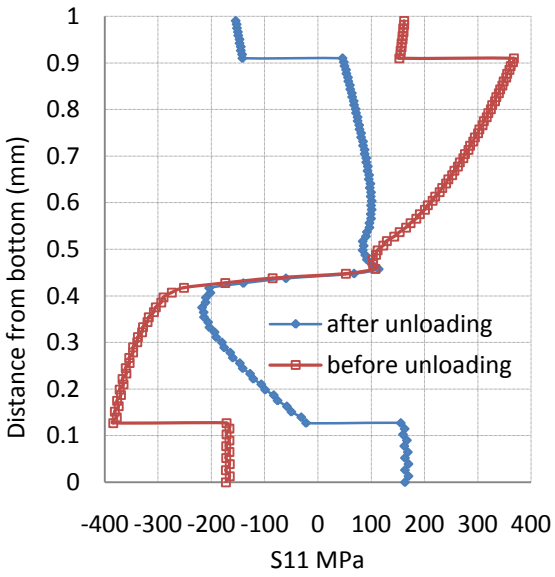

Figure 2.2.8: Top bottom clad S11 residual stress.

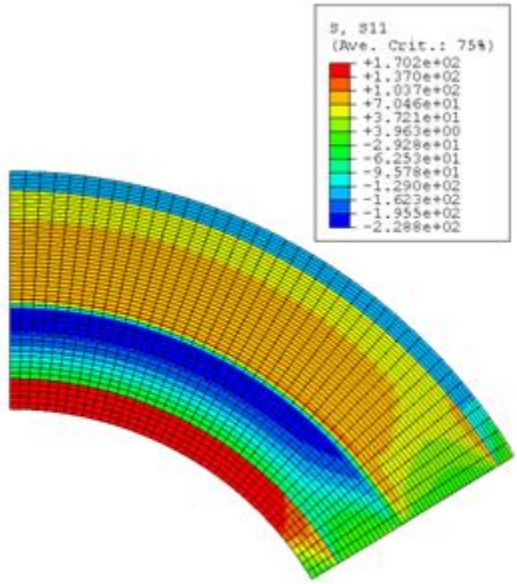

Figure 2.2.9: S11 contour after unloading for top bottom clad case.

The top and bottom 0.1 mm thick core material is replaced by cladding material to construct a 20% cladding volume fraction composite. Figure 2.2.8 illustrates S11 distribution before and after unloading along the left edge. Let's focus on the portion above the neutral surface. In the core session, the S11 distribution is similar to the pure core case before unloading. The neutral surface only shifted 0.05mm down from the geometry center. The discontinuity in the curve near the top indicates the cladding-core interface. The cladding area experiences small S11 stress state due to its low strength

nature. After unloading, the tensile stress reduces in the core, and the cladding area is completely in the compressive state. Overall, however, the tensile residual S11 stress in the core is higher than the pure core case. Moreover, at the interface between the core and cladding, residual S11 stress in core is still tensile 46.1 MPa while it is compressive -24.8 MPa at the same location in pure core case. The magnitude of compressive S11 residual stress in the cladding, 141.8 MPa at the interface, is much higher than it is for the same location, 14.5 MPa, in the pure cladding case. The mechanism explaining the compressive residual stress at top surface for pure core case applies to this phenomenon as well. With the same elastic modulus and plastic deformation, the recovered strain from unloading in low strength material is smaller than it is in high strength material. The plastic strain values in both the composite case and the pure core case are the same because of the 60 degree pure bending. At the top surface, the recovered strain in cladding is less than it is in the pure core case. While the core portion tends to shrink as much as it does in the same location in the pure core case, the outer layer starts to resist the spring-back of the right cross section earlier than it does in the pure core case. The significant difference between the shrinkage of the outer layer material itself and the shrinkage caused by the central portion and straight right edge plane causes less reduction of tensile stress in core section and more compressive stress at the top cladding than the pure core case and pure cladding case respectively during unloading. For the section below the neutral surface, the same mechanism caused less reduction of compressive stress in the core portion and more tensile stress than the pure core case and pure cladding case respectively.

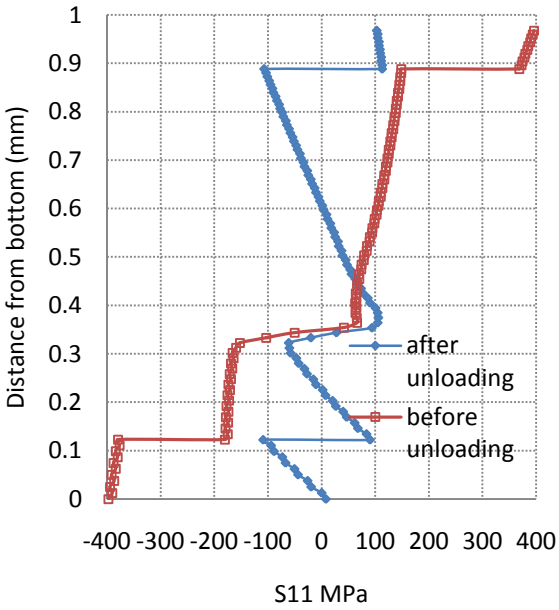

Figure 2.2.10: Top Bottom core S11 residual stress.

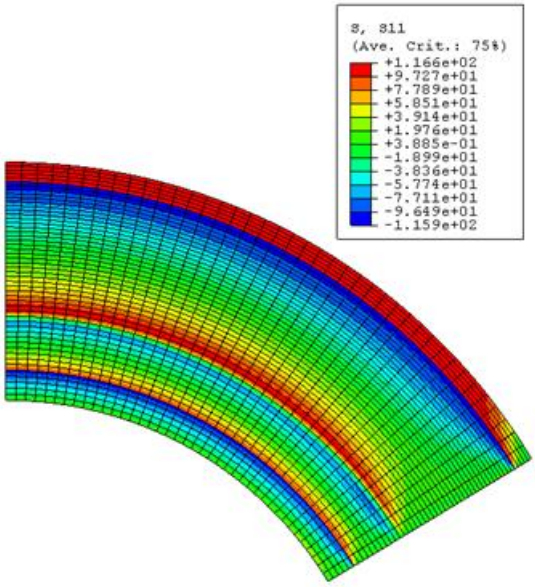

Figure 2.2.11: S11 contour after unloading for top bottom core case.

In this set of simulation, the core material is placed at the top and bottom surface and the cladding material is placed at the center. Before unloading, the S11 distributed similarly as it does in the pure cladding case in the central portion as shown in Figure 2.2.10. However, the neutral surface is shifted 0.15mm down verses 0.08mm in the pure cladding case. The stresses at the outer layers have higher magnitude compare to the central session due to high strength of the core material. As demonstrated in the shrinkage interaction between outer layers and central portion above, the recovered strain for high stress outer layer in this case during unloading is relatively large. With the small recovered strain for the soft center, the shrinkage caused by the recovery of the outer layers even surpasses the shrinkage induced by the recovery of the soft center and straight right edge plane. In contrast to the pure material and hard center, soft outer layers cases,

the center portion resists the spring-back of the outer layers during unloading. For the portion above neutral surface, the central part is further compressed and the tensile S11 stress is less reduced at the top layer comparing to the pure cladding case and pure core case respectively. The same phenomenon applies to the bottom portion as well. For instance, the S11 residual stress for the soft material at the outer layer and center interface is -107 MPa for top-bottom core case comparing -14.8 MPa for pure cladding case. The S11 residual stress for the hard material at the interface is 113.17 MPa while it is -30 MPa for the pure core case.

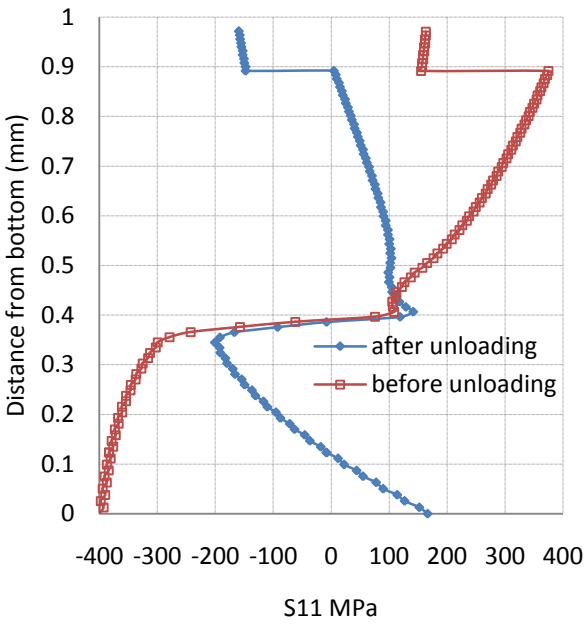

Figure 2.2.12: Top clad only S11 residual stress.

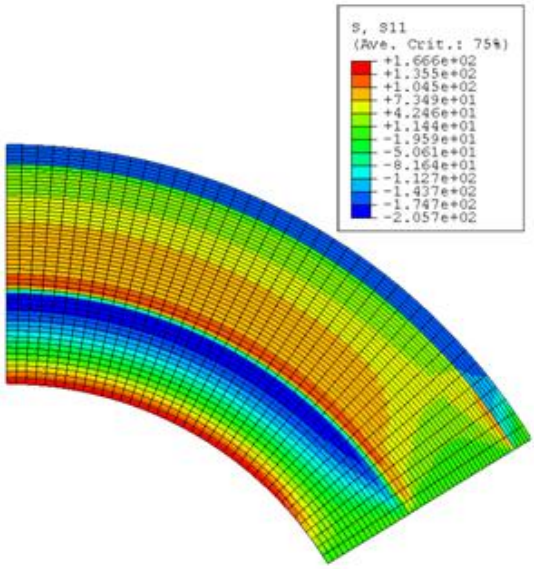

Figure 2.2.13: S11 contour after unloading for top clad case.

Figure 2.2.12 is the S11 distribution for sheet with cladding material only at the top surface. The section above the neutral surface is compared with the top-bottom

cladding case and the part below the neutral is compared with the pure core case due to the same material composition. Before unloading, the curve above neutral surface is almost identical in the case when both top and bottom are cladded. Comparing with the top-bottom surface cladded case, the only difference is the further downshift of the neutral surface, which goes to -0.094mm, due to the asymmetric pattern of the cladding material. The curve below the neutral is similar to the pure core case as well. After unloading, although the residual stress in the top surface is close to the curve in Figure 2.2.8, the S11 is further reduced to 4.8 MPa compared with 46.1 MPa in the symmetrically cladded case. Comparing 210 MPa in the pure core case, the residual stress at the bottom surface is 152 MPa. The change of S11 stress in core material after unloading should be a result of further down shifted neutral surface.

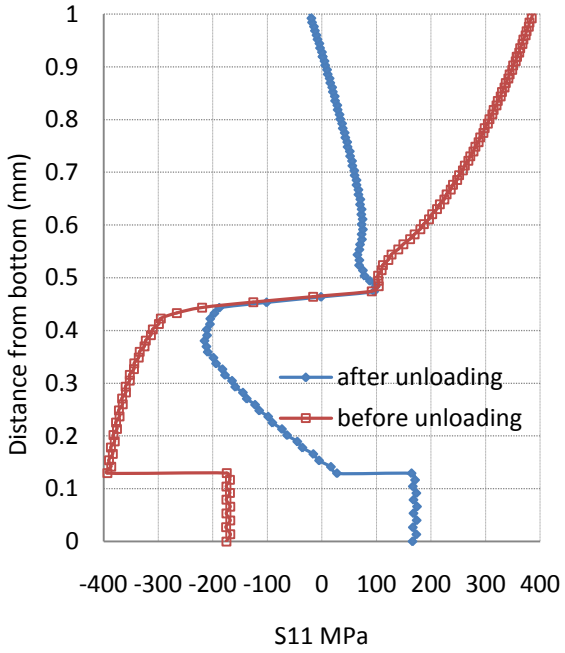

Figure 2.2.14: Bottom clad only S11 residual stress.

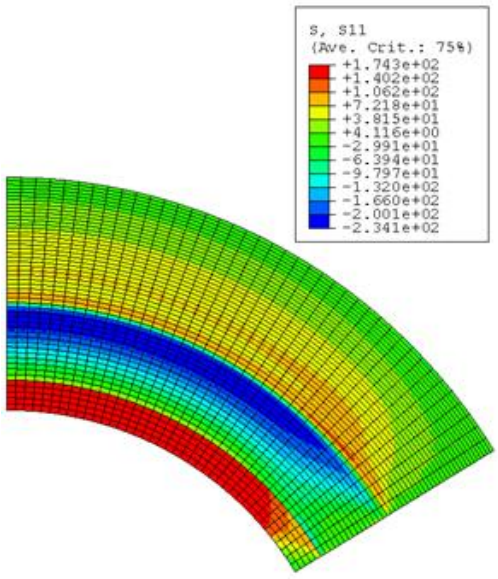

Figure 2.2.15: S11 contour after unloading for bottom clad only

The cladding material is then placed at the bottom layer only. Similar as the case in which only the top is cladded, the stress is very close to the top half of pure core case and bottom half of top-bottom cladded case accordingly. The down shift of the neutral surface is reduced to -0.036mm by the bottom cladding. This change of the neutral surface caused less compressive residual stress at the top and bottom in the core material. Interestingly, the residual stress is 27.8 MPa in the core and 164.2 MPa in the cladding at the interface comparing to -31.3 MPa and 155.4 MPa respectively in the sandwiched case.

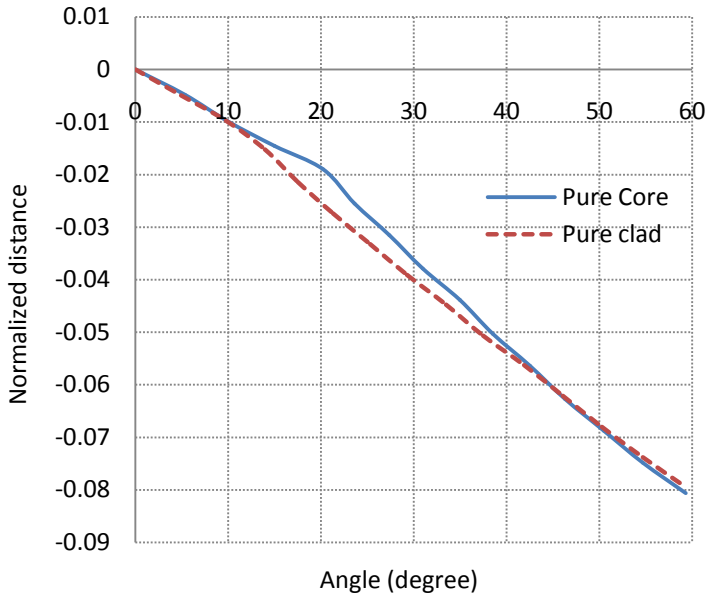

Figure 2.2.16: Neutral axis to center distance vs. angle plot for pure core and pure clad.

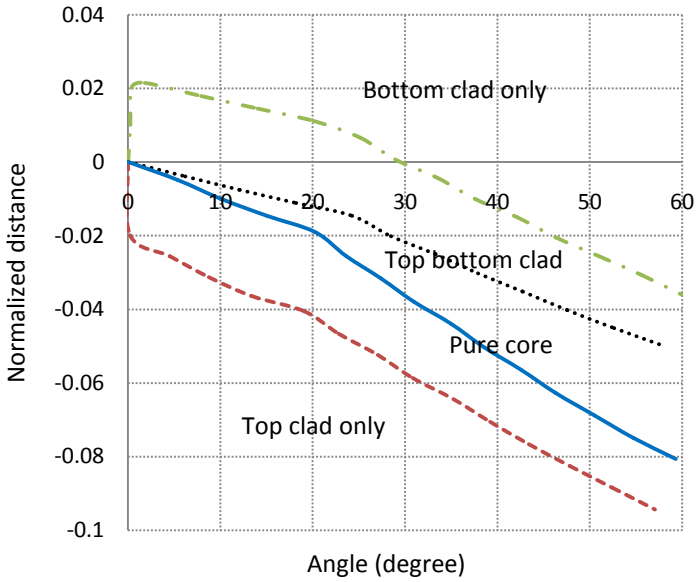

Figure 2.2.17: Neutral axis to center distance vs. angle plot for composite cases.

The neutral surface is down shifted more or less in all the cases discussed above. Figures 2.2.16 and 2.2.17 reveal more detailed history of the movement of the neutral surface during the bending up to 60 degrees. Since the movement of the neutral surface is within a small range of less than 0.1mm, it is sensitive to the change of thickness. Therefore, the actual shift distance is normalized by the current thickness for better comparison. In Figure 2.2.16, the movements of the neutral surface of the pure core and pure clad material cases are put into comparison. Although there is little discrepancy from 9.7 to 41degrees, the two curves basically overlap each other and reach -0.08mm at the end of bending. Figure 2.2.17 shows the history of neutral surface shift with different composites. Compared with the pure core case, the top-bottom cladding case reveals a less observed slope for descending. The soft cladding material at the top and bottom surfaces experiences less stress and exerts less influence to the composite than pure core

case. The effective thickness can be seen to be reduced and therefore, results in a slightly down shift of the neutral surface, which moves to -0.05mm from the geometric center. When the cladding material is only placed at the top layer, the effective part of the composite is shifted downward. As shown in Figure 2.2.17, the curve of top cladding only case drops to -0.02 at the very beginning of the bending, and gradually decreases to negative 0.094mm as the bending proceeded. Similarly, the soft cladding material at the bottom shifts the effective part upwards. The neutral surface moves to 0.02mm right after the bending started and descended to -0.036mm at the end of bending. The slopes in cases of top cladding only and bottom cladding only cases are more gradual than they are in the pure core case but steeper than they are in the top-bottom cladding case according to the amount of the hard core material in the composites.

During the spring back of plane strain bending, the curvature and the length of the sheet will change. The curvature is usually the measure of spring back since the change of length is negligible. The general equation predicting spring back is:

$$\Delta K = \frac{M(1-v^2)}{IE} \qquad (2\text{-}2\text{-}1)$$

and

$$\Delta K = \frac{1}{R^b} - \frac{1}{R^a} \qquad (2\text{-}2\text{-}2)$$

where R^b is the radius of the sheet before unloading and R^a is the radius after unloading.

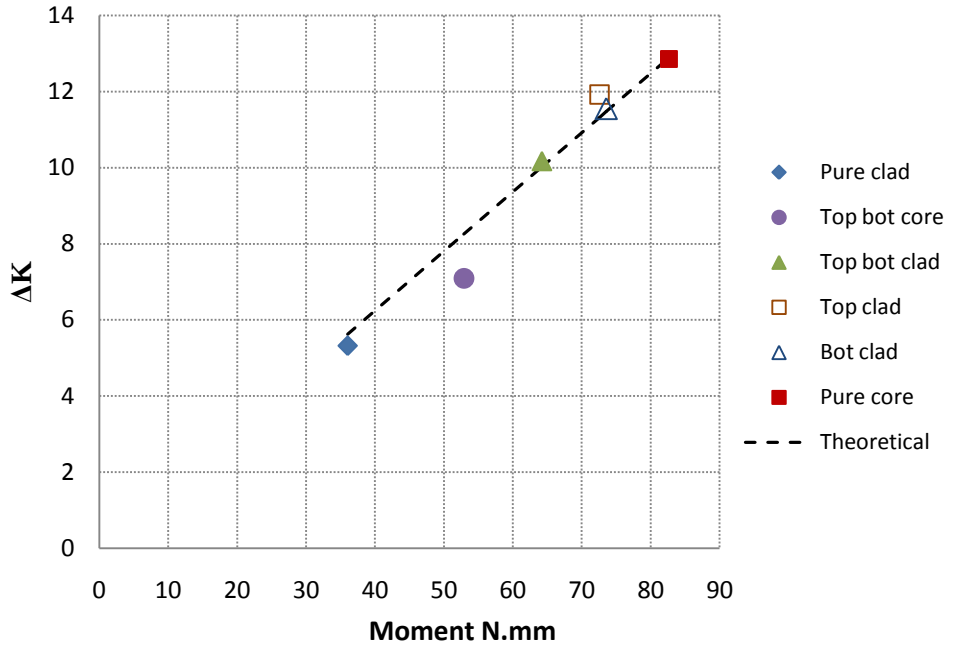

Figure 2.2.18: Pure bending ΔK vs. bending moment.

The ΔK of all the cases in pure bending is plotted against the associated bending moment in Figure 2.2.18. The theoretical value of ΔK calculated from equation (2-2-1) based on the moment is plotted as a dashed line in Figure 2.2.18. Clearly, the data points of various cases distribute closely to the theoretical line except for little offset in top bottom core case. Therefore, the results agree with the theory. According to the equation and the results, spring back is a linear function of moment. The slope of the linear function is not affected by the structure of the composition. Poisson's ratio, Young's modulus and moment of inertia will change the slope. In Figure 2.2.18, the pure clad case has the lowest moment and spring back whereas the pure core case has the highest spring back according to the strength of the materials. The composite cases are found between the two extreme cases.

2-2-3. Hydro forming

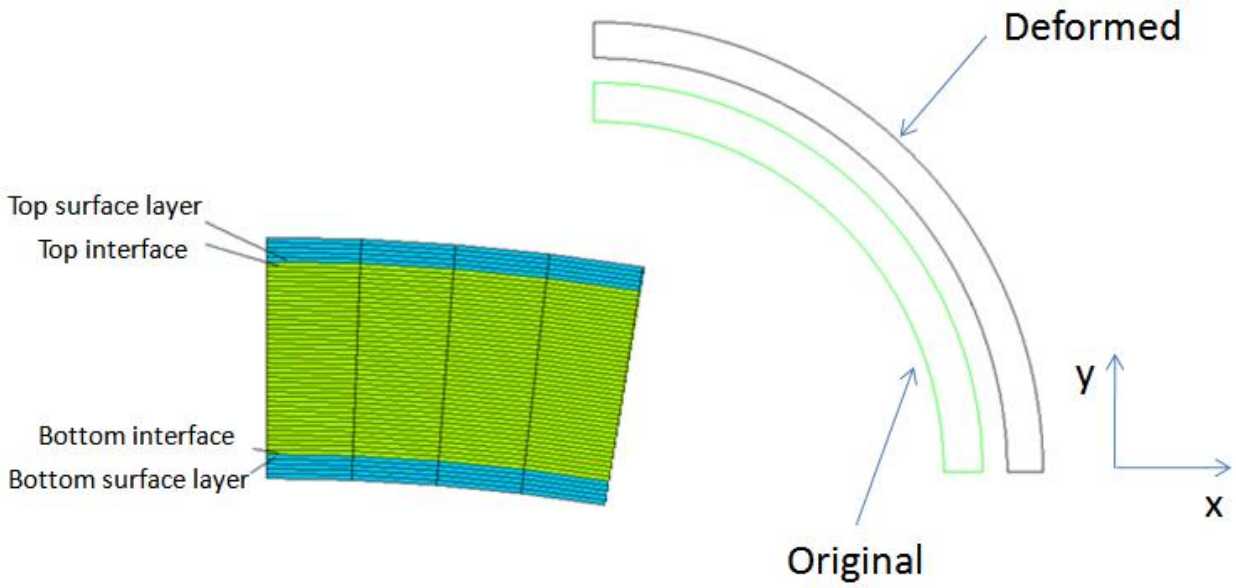

Figure 2.2.19: Schematic of composite hydroforming process.

A circular tube undergoing a hydroforming process is modeled in this section. The ends of the tube are sealed and pressurized liquid is pumped into the tube. The inner diameter of the tube is expanded to 140%, which means from 9mm to 10.63mm. The tube is assumed to be infinitely long into the page and a quarter of the cross section is modeled due to the symmetry of the tube geometry and load as shown in Figure 2.2.19. The left end of the top is constrained in x direction and the bottom end is constrained in y direction. The thickness of the tube is 1mm and 0.1mm thick of material from the top surface and bottom surface is partitioned and different materials can be assigned to the top layer, bottom layer and the center portion to examine the effect of material composition on hydroforming. The isotropic power law hardening materials used are core material featuring Young's modulus of 70 GPa, Yield stress 110 MPa, n=0.3 and K=500

MPa, and cladding material which has Young's modulus of 70 GPa, yield stress 43 MPa, n=0.204 and K=183 MPa.

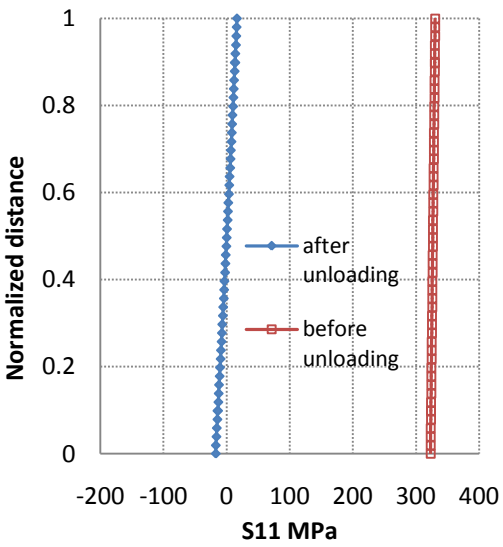

Figure 2.2.20: S11 distribution for pure core

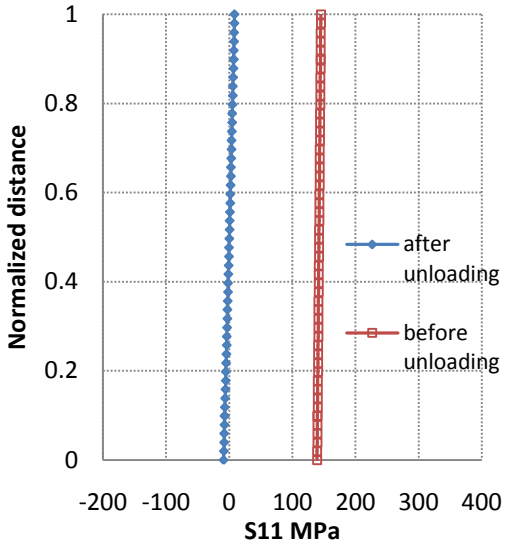

Figure 2.2.21: S11 distribution for pure clad case.

In Figure 2.2.20, the core material is assigned to the whole model and the S11 stress distribution along the thickness direction at the top right end is plotted. Due to the significant reduction of thickness during the hydroforming process, the locations of the data points are normalized by the instantaneous thickness and this method is adapted in the subsequent analysis. As shown in Figure 2.2.20, the S11 stress does not vary much across the thickness before unloading. It is 322 MPa at the bottom and 330MPa at the top with linear distribution. After unloading, the hydro-static pressure in the tube wall is released and the thickness is recovered from 0.8611mm to 0.8628mm. The reduction of inner radius, which goes from 10.632mm to 10.583mm, and the unloading of the material push the bottom part of the sheet into compressive residual S11, which is -17.26 MPa.

The resistance of the shrinkage caused by the compressive stress at the bottom leaves the top surface in tensile residual S11 with the value of 16.18MPa. The neutral surface is 0.42 of the normalized distance from the bottom. The material of the whole model is then changed to cladding material and the stress distribution is plotted in Figure 2.2.21. Although the trend is the same, the magnitude of the S11 before unloading and the residual S11 after unloading is significantly smaller compared with the pure core case because of the softer nature of the cladding material. Before unloading, the S11 stress is 139.2 MPa at the bottom and 145 MPa at the top surface. The residual S11 is -8.83 MPa at the bottom surface and 8.3 MPa at the top after unloading.

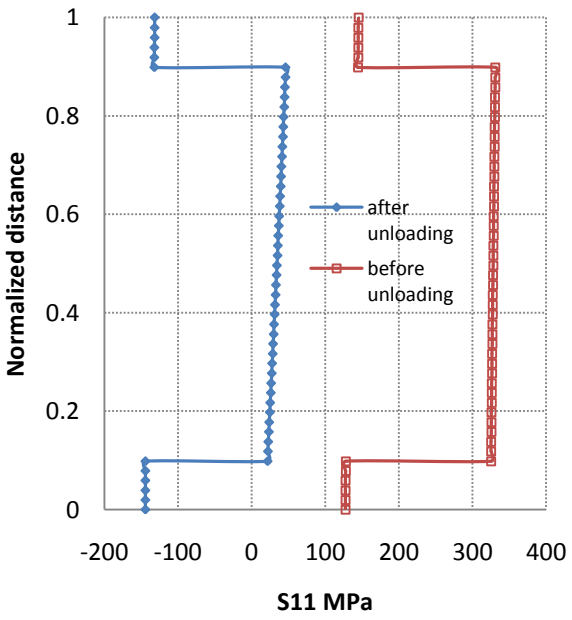

Figure 2.2.22: S11 distribution for top bottom clad composite.

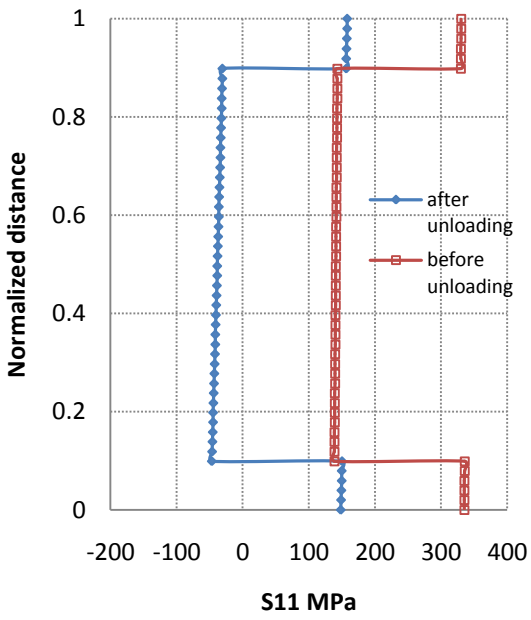

Figure 2.2.23: S11 distribution for top bottom core composite.

The cladding material is assigned to top layer and bottom layer while the central portion is consisted of core material. As shown in Figure 2.2.22, S11 is 127 MPa at the bottom surface and 145 MPa at the top. The step of the curve indicates the clad-core interface. The S11 at the center core is linearly distributed from 325 MPa at bottom clad core interface to 330 MPa at the top clad core interface. Having the same initial strain, the recovered strain during unloading for soft cladding material is smaller than it is for the hard core material. Similarly, as the shrinkage mechanism described in pure bending, the top and bottom layers are pushed to compressive residual S11,-144 MPa, and the core is left to tensile residual S11, -131 MPa. As explained in pure core hydroforming case, the reduction of inner radius and release of hydro-static pressure induce more compressive residual stress at the bottom compared to the top. Similarly, the residual S11 at the top clad core interface is 46.35 MPa, which is more tensile than 22.17 MPa at the bottom clad core interface. The materials at the top and bottom layers and the center are then switched. Figure 2.2.23 is the S11 plot for cladding material at center and core material at top bottom surfaces. During unloading, significant shrinkage caused by the considerable recovered strain of strong core material at the top and bottom layers pushes the center part to compressive residual S11. The residual S11 in the softer material at top clad core interface is -30.57 MPa, and it is -46.53 MPa at the bottom clad core interface. The interaction between the center and the top bottom layers also pushes the hard material to tensile residual S11. The residual stress at the top surface is 157.9 MPa while it is 148.3 MPa at the bottom surface.

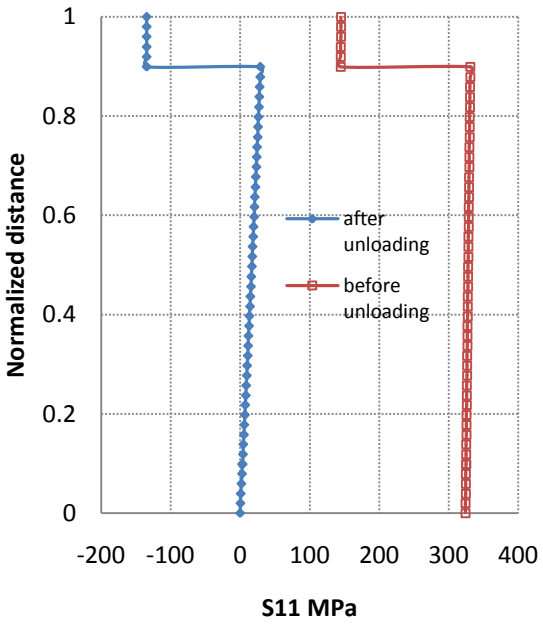

Figure 2.2.24: S11 distribution for top clad only composite.

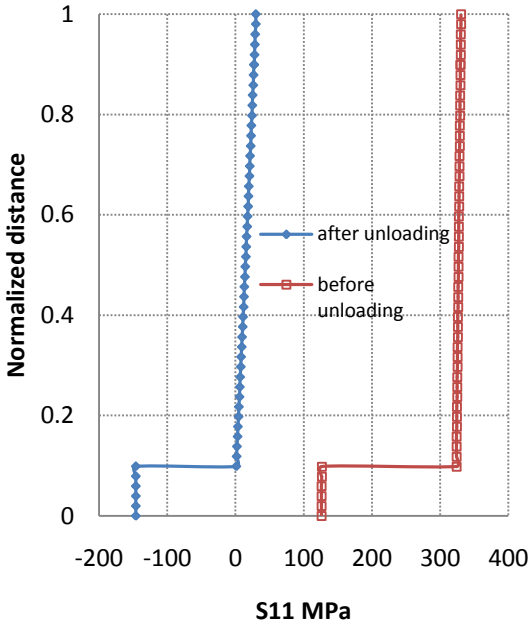

Figure 2.2.25: S11 distribution for bottom clad only composite.

The cladding material is assigned to the top layer only while the rest of the sheet is consisted of core material. In the core portion, the S11 ranges from 324.29 MPa at the bottom to 330.95 MPa at the top clad core interface before unloading. Again, due to the soft nature of the cladding material, the stress at the top surface is 145 MPa. After unloading, the large shrinkage of the core pushes the top layer to -134 MPa while the interaction between the two materials leaves 29.26 MPa in the core at the interface and 0.11 MPa at the bottom surface. When the cladding material is assigned to the bottom layer only, the trend is the same as it happens in previous cases. The S11 stress at the bottom surface is 125.8 MPa before unloading. It varies from 323.2 MPa at the interface

to 330 MPa at the top surface. After unloading, S11 is 29.9 MPa at the top surface and 1.17 MPa at the interface while it reaches -145.8 MPa at the bottom surface.

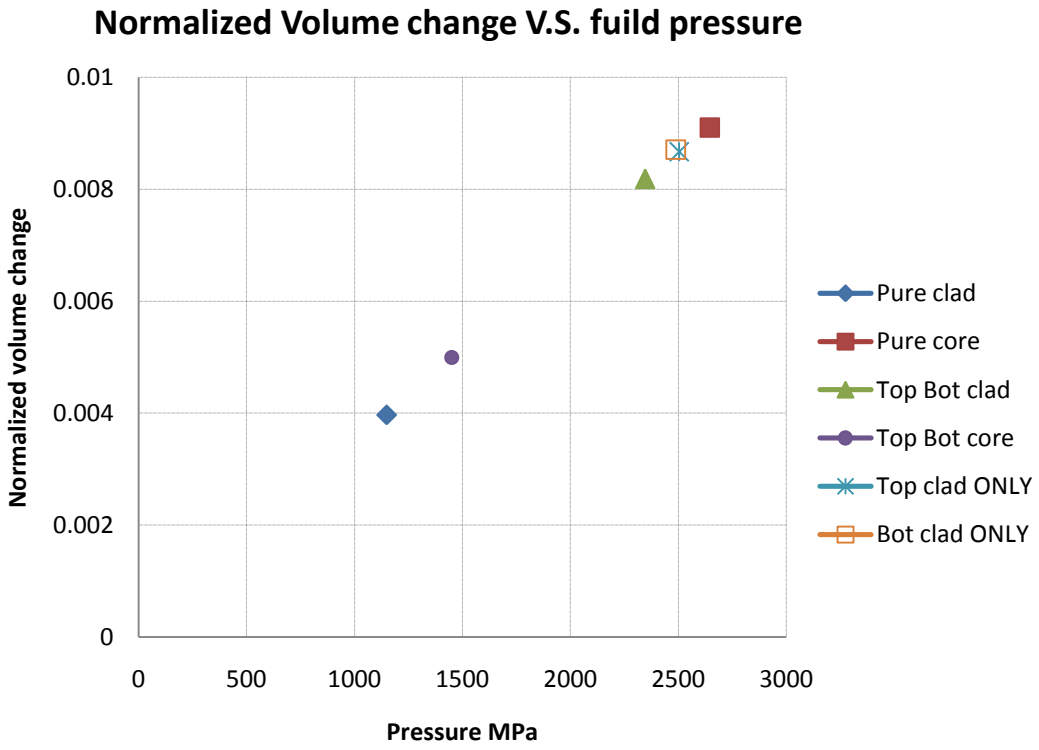

Figure 2.2.26: Relationship between normalized volume change and pressure in hydroforming.

During the hydro forming and unloading, the inner volume of the tube changes. The change of the tube inner volume after unloading is normalized by the tube inner volume before unloading, and the absolute value is plotted in Figure 2.2.26. Clearly, the normalized volume change is proportional to the fluid pressure, but the slope of the linear relation is not affected by the material composition. Because of the strength and recovered strain during unloading of the material, the pure clad case has the smallest

normalized volume change and fluid pressure whereas the pure core case has the largest normalized volume change and pressure.

2-2-4 Conclusion

Sixty degree pure bending and spring back of a segment of sheet under plane strain condition is modeled by FEA. The boundary condition and load are induced by MPC to ensure pure bending conditions. Different material compositions are also examined. The high hydro-static pressure below the neutral surface causes asymmetric distribution of S11 stress along the thickness at the end of bending. After unloading, the shrinkage difference caused by the unloading of outer layer and center results in compressive and tensile residual stress at the top surface and bottom surface, respectively, in pure material cases. More compressive residual S11 at the top and more tensile residual S11 at the bottom are produced by replacing the outer layers by soft cladding material. As the bending angle increases, the neutral surface is shifted down. The rate and final value of this shifting are affected by material properties and material compositions. The change of curvature during spring back is a linear function of bending moment while the slope of the linear relation is independent of the compositional structure. Young's modulus, Poisson's ratio and moment inertia of the sheet will affect the slope of the linear function. The obtained results are compared with analytical solution and they match with each other well.

Furthermore, aspects such as the stress distribution across the thickness, and volume change after unloading of a circular tube whose internal volume is expanded to 140% in hydroforming process are also studied. Due to the symmetric nature of the geometry and the load, one quarter of the tube is modeled. In pure material cases, the stress varies little across the thickness at the end of hydro forming process. After unloading, the reduction of inner radius during release of hydro-static pressure leaves tensile residual S11 at the top surface and compressive residual S11 at the bottom. The magnitude of the residual stress is proportional to the strength of the material. Adding the soft cladding material at outer surfaces causes more compressive residual stress at the cladding layers. The volume change after unloading is proportional to the fluid pressure inside the tube, and the slope of the linear relation is independent of the material compositions.

Chapter 3 Strain hardening improvement by corrugated reinforcement

3-1. Introduction

Strain hardening is a measure of material ability to distribute strain uniformly. Large strain hardening is highly valued and desired in material science and mechanical engineering for the reason that it can delay necking and improve formability for sheet metals and composites. According to Considere's theory, necking occurs when the strain hardening curve and stress strain curve intersects as was shown in Figure 1.10. Shifting up the strain hardening curve or shifting down the stress curve can delay necking. Down shifting the stress curve would reduce the strength and decrease load carrying ability. Therefore, improving strain hardening without compromising strength has been a special interest to researchers. Many methods have been employed in solving this problem including altering the microstructure by metallurgical process, changing mechanical behavior by composites [Chen et al. (2010)], compositionally graded [Bouaziz et al. (2008)] or architectured materials [Embury et al. (2010)], Twinning Induced Plasticity [Mirko et al. (2003); Bouwhuis et al. (2010)] and Transformation Induced Plasticity [Dan et al. (2007)].

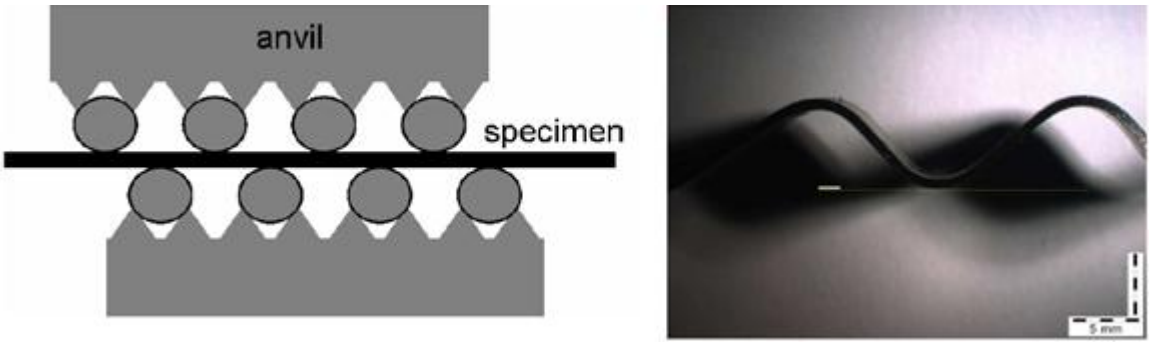

(a) (b)

Figure 3.1: Illustration of the device making corrugation and example of corrugation. (a) Device used for making corrugated samples; (b) Example of corrugation. [Bouaziz et al. (2009)]

Bouaziz et al. introduced a new efficient method for improving strain hardening rate by embedding corrugated reinforcement in steel matrix [Bouaziz et al. (2009)]. The independent corrugation strip is made by compressing a flat steel strip between two anvils as shown in Figure 3.1(a). The corrugation geometry can be changed by different roller sizes and spacing. In uniaxial tensile process, the corrugations bring additional elongation to enhance the necking strain. In [Bouaziz et al. (2009)], the corrugation is then combined with matrix, and the tensile process is simulated by Finite Element Modeling. Figure 3.2 is the stress strain curve of the composite. The stress for flat strip reinforced composite is constant after the specimen reaches plastic region due to the perfect plastic material property for both the reinforcement and matrix. The corrugation reinforced cases have slightly low stress at the end of elastic region, but the stress continues to increase as the composite is further strained due to the flattening of the corrugated reinforcement. The h/p value is the ratio of the amplitude and the period. It measures the extent of folding of

the corrugation. For the strain hardening rate versus strain curve as shown in Figure 3.3, the strain hardening rate is zero for flat strip reinforced composite while it is significantly improved as the composite is strained in the corrugated cases. The strain hardening peaks at a different strain value according to the corrugation structure. The high h/p value is associated with high peak strain. The straightening of the corrugation provides additional strain hardening especially at large strains and hence improved the necking strain of the composite. In this chapter, detailed investigation of the corrugation reinforced composite is conducted. The problems are approached by Finite Element modeling. Firstly, tensile behavior of independent corrugation strip is studied and the optimal geometry is examined. After that, the results of independent corrugation study are incorporated with the matrix, and the necking strain improvement of the corrugation reinforced composite is reported.

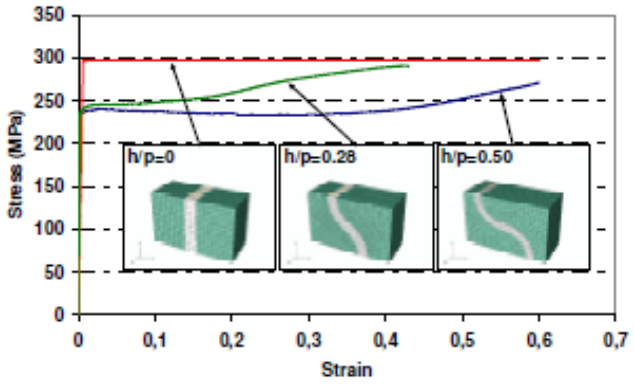

Figure 3.2: Stress strain curve for flat reinforced and corrugation reinforced composites.

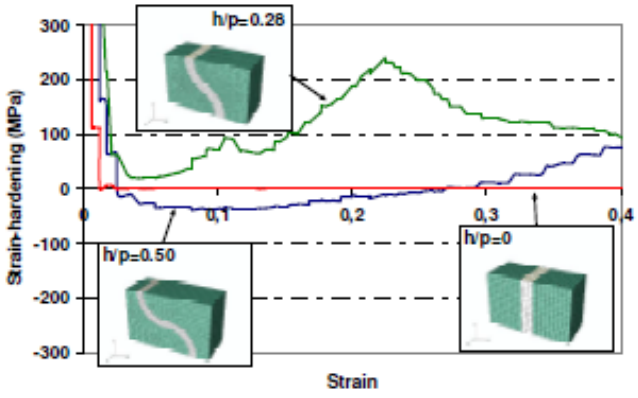

Figure 3.3: Strain hardening curve for flat reinforced and corrugation reinforced composites.

3-2 Uniaxial tensile behavior of independent corrugated strips

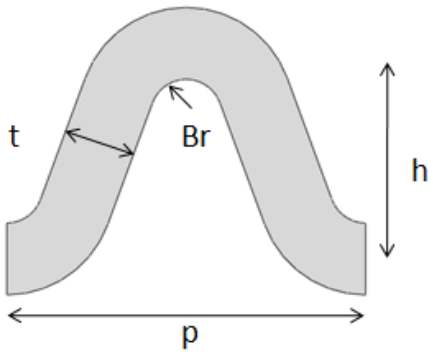

Figure 3.4: Schematics of a corrugation.

The ultimate goal of designing a corrugated reinforcement is that it should provide high necking strain without compromising the strength of the composite. With this in mind, the geometry of the corrugation is thoroughly studied. As shown in Figure

3.4, the parameters determining a corrugation involve shape, bend radius Br, amplitude h, period p and thickness t. The h/p value as mentioned earlier can be a useful normalized parameter.

To recall in [Bouaziz et al. (2009)], corrugation is made by pressing a flat steel strip between two anvils. Residual stresses exist and the strain distribution is not uniform throughout the corrugation. Another way to make the corrugation is casting. The melted metal can be poured into modes and afterward, the corrugation is formed. In contrary to the pressed case, the residual stress is nearly 0 and strain is uniformly distributed through the whole cast corrugation. The cast corrugation and the pressed one are compared in order to examine the effect of residual stress, which is induced in pressing process, on the tensile behavior. As shown in Figure 3.5, a flat strip, which has a thickness of 1mm, length of 27.5mm and infinite depth into the page, is clamped at both ends. The friction coefficient between the strip and clamp is 0.1, and the clamping force is 250N/m. The rollers are placed 5.34mm apart and they are assumed frictionless. The distance between the first roller and the clamp is half of the roller spacing. The material property for the strip is obtained by curve fitting the interstitial free steel uniaxial tensile behavior in [Bouaziz et al. (2009)]. The power law hardening parameters are: Young's modulus= 210 GPa, Poisson's ratio= 0.3, yield stress =163 MPa, K=650 MPa and n=0.27.

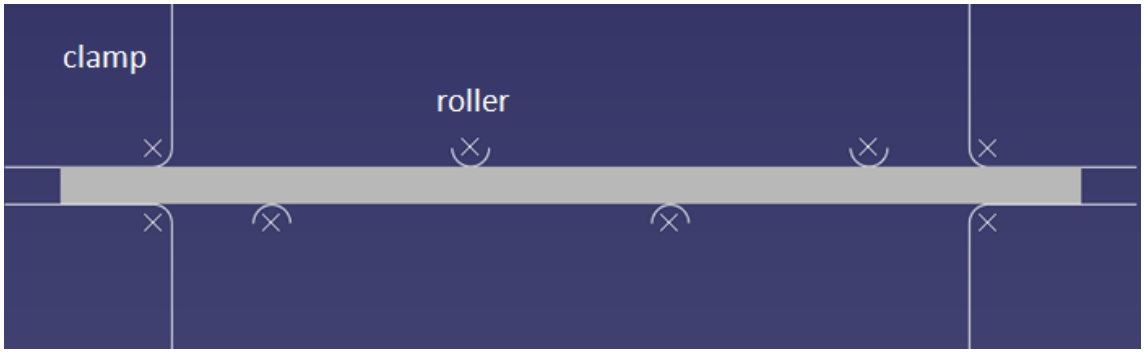

Figure 3.5: Schematics of the pressing process for making corrugations.

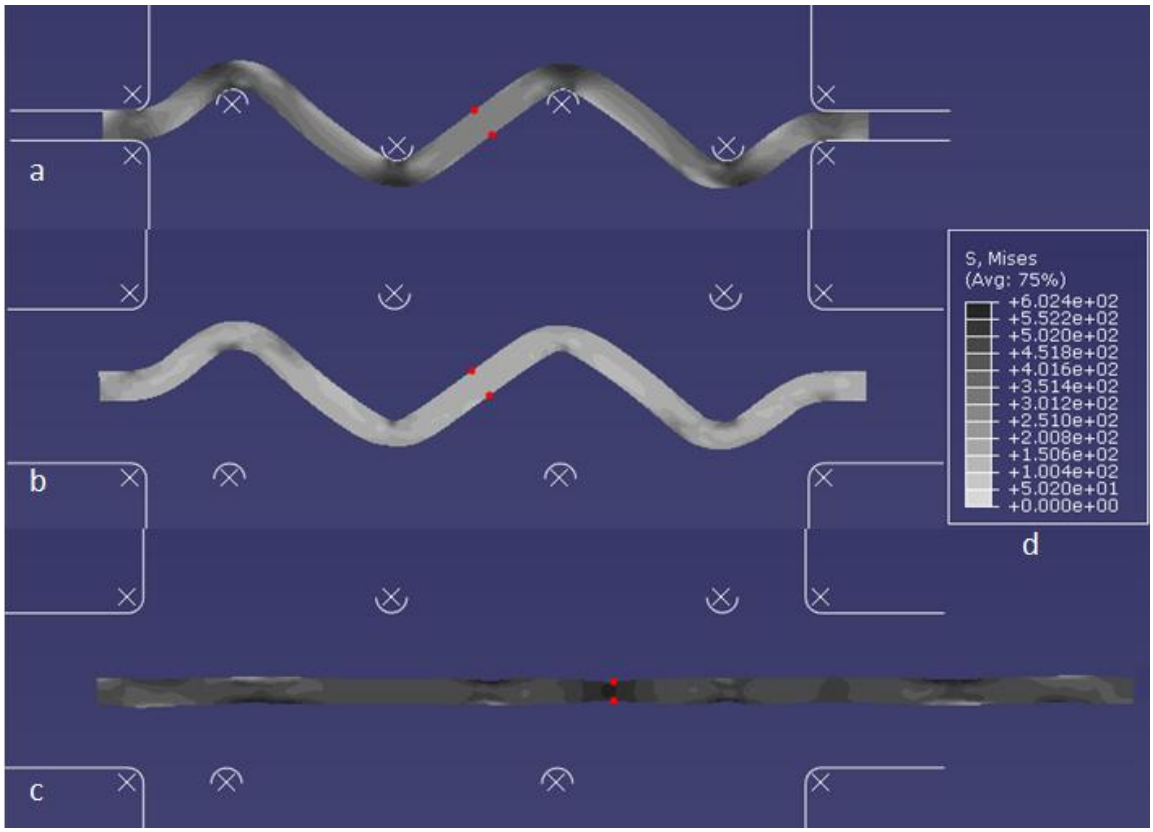

Figure 3.6: (a) End of the pressing process; (b) Removal of the clamp and rollers; (c) Stretching of the corrugation up to necking.

As illustrated in Figure 3.6(a), the corrugation is formed when the rollers move up or down to compress the strip. The vertical displacement for rollers is 1.675 mm, so the amplitude for the corrugation is 1.675 mm × 2 = 3.35 mm. The period for the

corrugation is twice the spacing between rollers, which is 5.34 mm × 2=10.68 mm. The h/p value is 0.313. The roller and also bend radius is 0.5mm. In Figure 3.6(b), the rollers and clamps are removed. The Von Mises stress contour is lower than it is in Figure 3.6(a) due to the unloading. Spring back causes the slight change of geometry, but the difference is negligible. Same as in Figure 3.6(a), the stress state at the bend is still higher than the straight portion. In Figure 3.6(c), the left end of the corrugation is constrained in x direction while the right end is pulled until necking occurs. The red dots indicate the location of necking. As shown in Figures 3.6(a) and 3.6(b), the necking occurs at the straight portion which is the least work hardened area during pressing process. The tensile behavior of the pressed corrugation is compared with the cast one, which has the same geometry but zero initial stress and strain distribution.

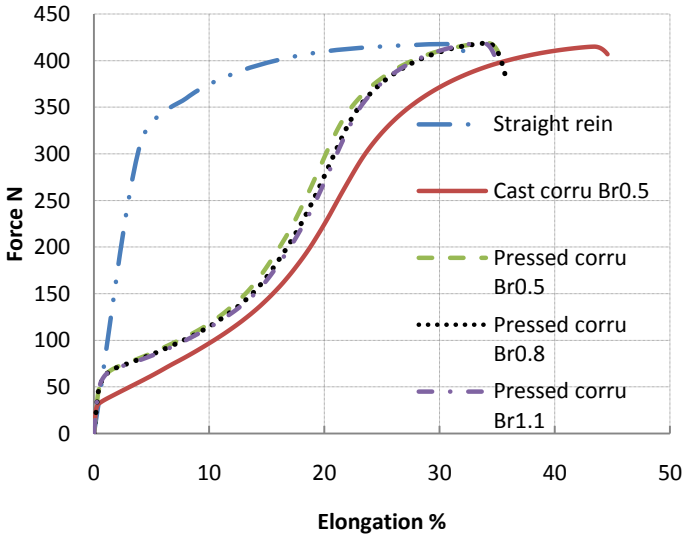

Figure 3.7: Tensile behavior comparison between cast and pressed corrugation.

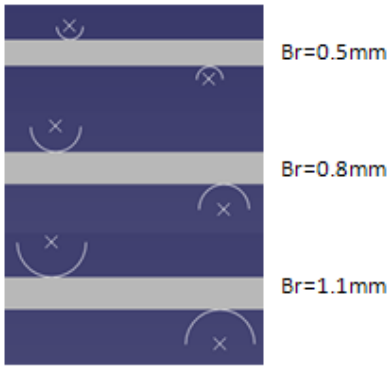

Figure 3.8: Schematics of different roller sizes.

In Figure 3.7, the force over elongation curve for the pressed corrugation is overall higher than the cast case due to the initial work hardening during the pressing process. Compared with the straight reinforcement, the pressed corrugation shows an improvement of necking strain by 34.12% elongation while the straight case necks at 30.8% elongation. However, the necking strain is significantly enhanced by cast corrugation at 43.4% strain, which is a 27% increase from pressed corrugation and 41% increase from the straight reinforcement. Consumed strain hardening during the pressing process results in less improvement of necking strain for pressed case compared with the cast one. The roller size is then changed to 0.8mm and 1.1mm to examine the bend radius effect of the pressed corrugation as shown in Figure 3.8. The force curves in Figure 3.7 for pressed cases overlap, indicating the tensile behavior is not sensitive to the bend radius for the pressed case. Increasing the bend radius will cause the reduction of stress at the bends, but it has little influence on the stress at straight portion where the necking occurs. Therefore, bend radius has negligible effect on the tensile behavior. Moreover, cast corrugation clearly demonstrates much more satisfying necking strain improvement than the pressed case while the maximum strength are the same. Cast corrugation will be used in the subsequent study.

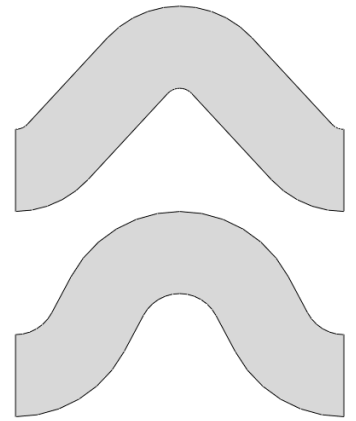

Figure 3.9: Shape comparison between Br=0.5 and Br=0.2.

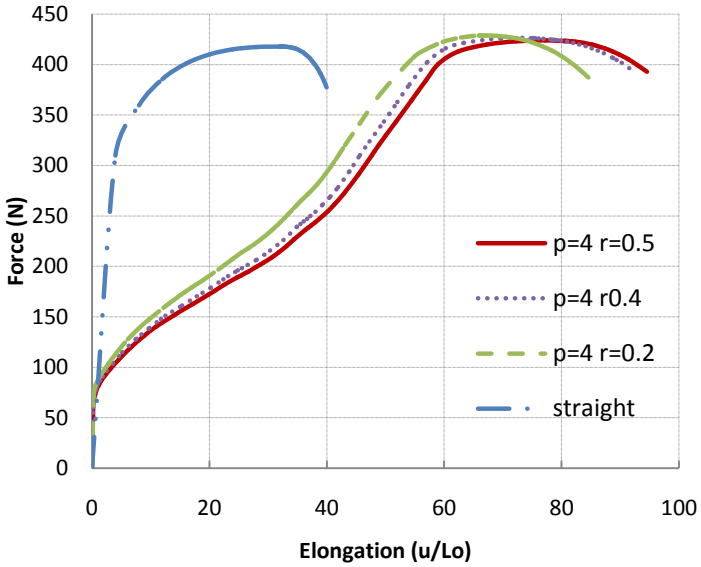

Figure 3.10: Bend radius effect on cast corrugation tensile behavior.

The bend radius effect of cast corrugation is first studied. The figure at the bottom in Figure 3.9 is the corrugation with bend of radius Br= 0.5 mm, and the figure at the top is the case with Br= 0.2 mm. Both cases are not pre-strained. The Br=0.5 case has area of 5.32 mm^2, maximum force 423 N and necking elongation of 77.18%. The Br=0.2 case has slightly smaller area of 5.17 mm^2, maximum force 428 N and 66.83% necking elongation. In Figure 3.10, straight case, Br=0.4 and Br=0.3 are added and compared with Br=0.5 and Br=0.2 cases. All the corrugated reinforcements have h/p=0.375 and period of 4. Due to the geometry constraint, the areas for corrugated cases are slightly different, but the maximum difference is only 2.9%. The straight reinforcement has the same amount of material and thickness as the corrugated reinforcement. Clearly, the corrugated cases show significant improvement of necking strain and similar maximum force compared with the straight reinforcement. According to Figure 3.10, high bend radius is associated

with high necking strain. Stress concentration at the bend during the stretching process induces this influence. Large bend radius causes low stress concentration and more uniformly distributed stress at the bend, leading to high necking strain. The maximum necking strain difference is between Br=0.5 case and Br=0.2 case, and 15.5% of improvement is observed. The maximum forces for all the cases are quite similar with the biggest difference for only 1.16%. The bend of radius demonstrated noticeable influence on necking strain, and little impact on strength.

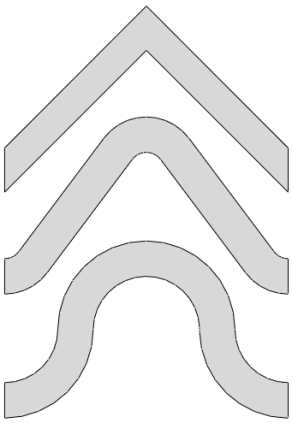

Figure 3.11: Schematics for triangular, arc and arc straight shape.

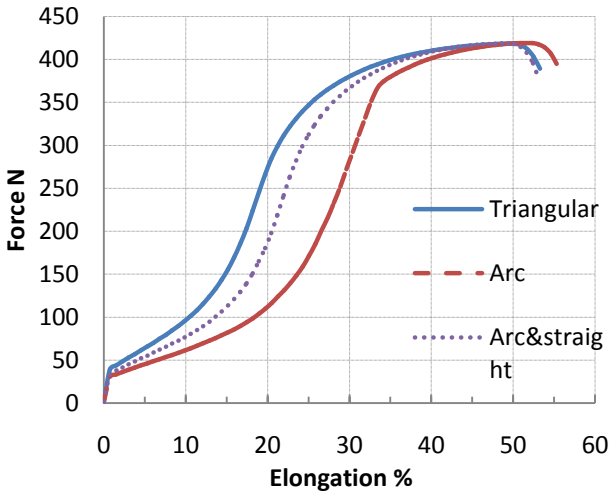

Figure 3.12: Tensile behavior comparison for triangular, arc and arc straight shape.

The shape effect is then studied. Three shapes, triangular, arc and straight with arc, are compared. As illustrated in Figure 3.11, the triangle shape is consisted of all straight parts with a sharp triangular intersection. The arc shape is made up by sections of arc. The two straight parts are joined by an arced bend in straight with arc geometry. The

triangular case tensile curve shows high initial stress with low necking strain while the arc case shows low initial stress with high necking strain in Figure 3.12. The stress and necking strain behavior for arc straight corrugation is in between the triangular case and the arc case. Among the three cases, high necking strain is associated with low strength. Therefore, the corrugation shape cannot produce the ideal reinforcement featuring high strength and high necking strain.

The period p and the amplitude h are the two major factors that mostly distinguish a corrugation. To determine the impact of p, the thickness is kept constant to 1 mm and the amplitude h is kept to 3mm while the period is changed from 4 to 12. The h/p value is decreased from 0.75 to 0.25 accordingly. The geometry for p=4 and p=12 are portrayed in Figure 3.13. As shown in Figure 3.15, the necking strain for p=4 case can reach 160% while the p=12 case can only reach 40%. The necking strain decreases as the p value increases due to the decreased h/p value. The engineering strain is normalized by dividing the necking strain for the x axis in Figure 3.16. Force is plotted against the normalized strain to show the load carrying ability for each case during the tensile process up to necking. Although the forces are the same at the beginning and the end, the higher p value case exhibits higher force compared with the lower p value case at the same normalized strain. As the p is increased, the h/p decreases and corrugation is more easily stretched to straight. The strength of the material plays an important role at early stage, and the tensile behavior is more close to the straight strip for high p cases. The large h/p case has high necking strain, but it is weaker compared with small h/p cases.

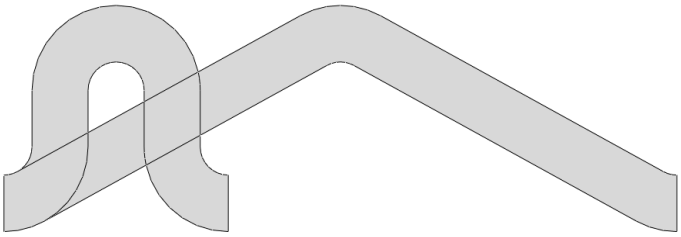

Figure 3.13: Schematics for corrugations with p=4, h=3 and p=12, h=3.

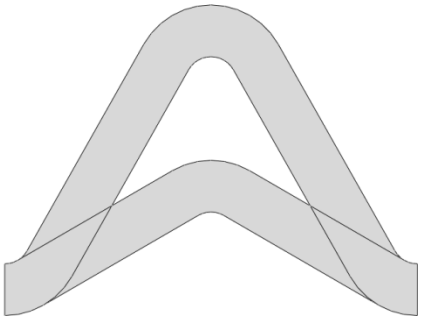

Figure 3.14: Schematics for corrugations with p=8, h=2 and p=8, h=5.

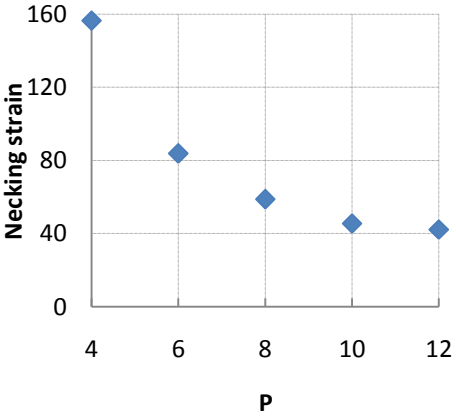

Figure 3.15: h=3, p effect on necking strain.

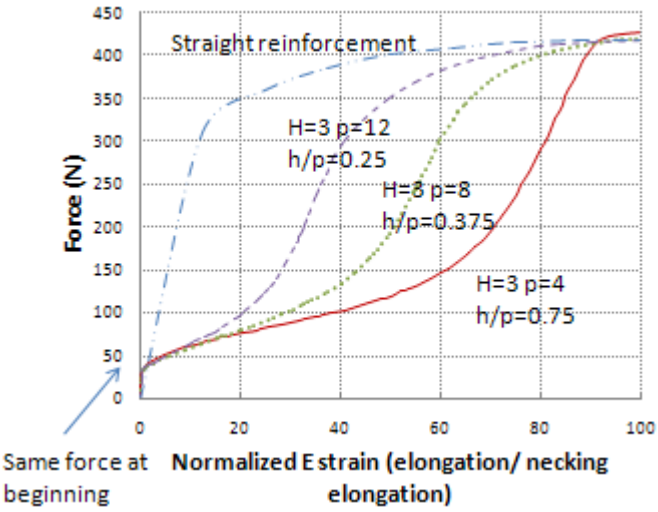

Figure 3.16: p effect on tensile behavior.

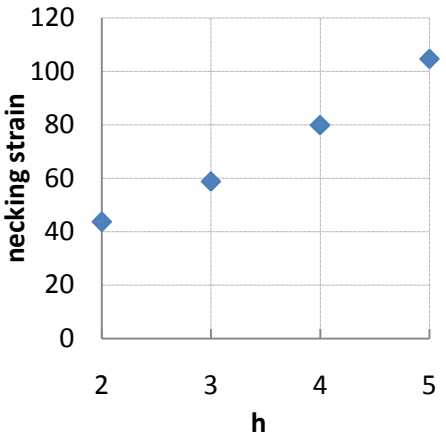

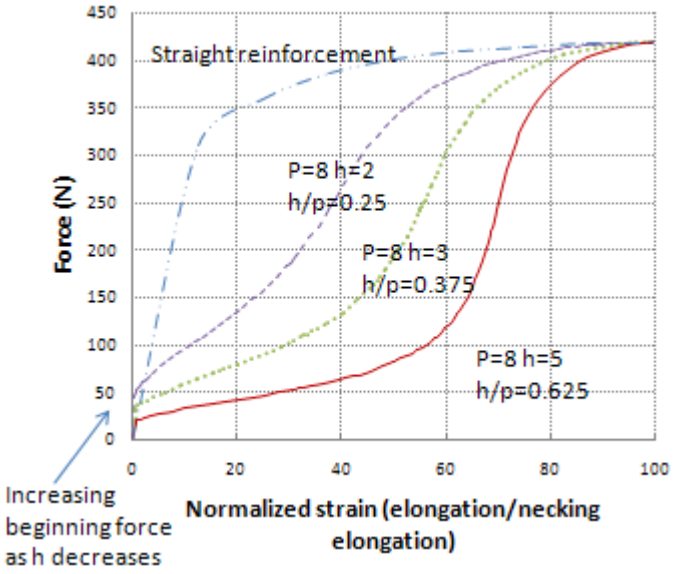

Figure 3.17: p=8, h effect on necking strain. Figure 3.18: h effect on tensile behavior.

The thickness and period are kept constant to 1 mm and 8mm to examine the effect of amplitude h on the corrugation. As shown in Figure 3.14, the amplitude is changed from 2 to 5 as the h/p ratio is increased from 0.25 to 0.625. The necking strain for h=2 case is 42% and 103% for h=5 case. According to Figure 3.17, the necking strain increases as the amplitude h increases due to more portion of the corrugation is folded up. In Figure 3.18, similar as the p changing cases, the force is higher for the small h/p case compared with large h/p case. The maximum forces before necking are the same for all the cases. However, unlike the same force at the beginning for constant h cases, higher force for smaller h/p value at the beginning is observed. In general, same trend is observed as in constant h varying p cases. High necking strain specimen is associated with low strength.

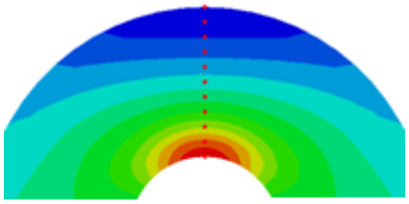

Figure 3.19: Location for S11 stress distribution.

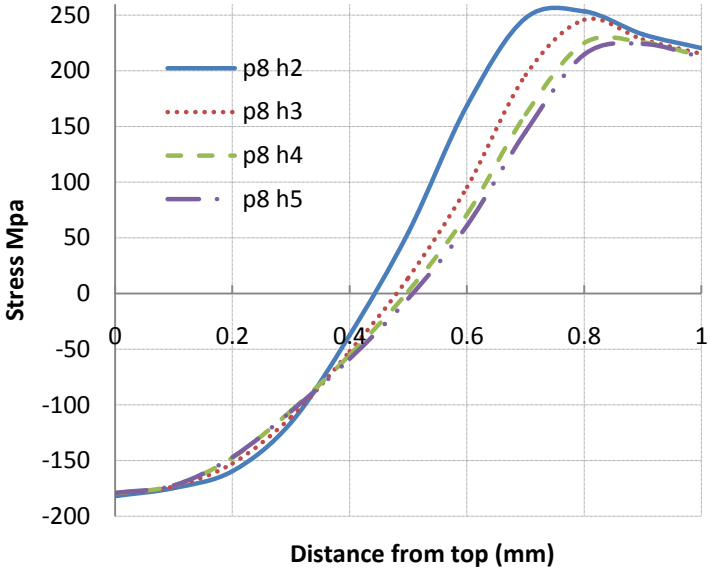

Figure 3.20: S11 stress distribution along the center of the bend.

To now more closely examining the initial stage where the forces are different in Figure 3.18. Figure 3.20 is the x direction stress distribution at the center of the corrugation bend shown in Figure 3.19. For h=3, 4, and 5, the S11 distribution are very close, especially for h=4 and 5. The curve for h=2 slightly differs from the others. When h is small, the influence of the thickness and bend radius is more pronounced. On the other hand, when h is large, those influences diminish, and the stress curves overlap. With the same S11 stress distributions, the moment required to unbend or bend the corrugation will be the same. In the tensile process of the corrugated reinforcement, the force is applied at the bottom bends along x direction. The moment at the top bend is equal to the force at the bottom bend, F, times the amplitude h as shown in Figure 3.21. To produce the same moment, small h needs large force F. In other words, the force required to stretch the

corrugation having small amplitude h is higher than it is for stretching the corrugation with high amplitude h. Therefore, the corrugated reinforcement with same thickness, same h/p value, and small amplitude is stronger than it is with large amplitude.

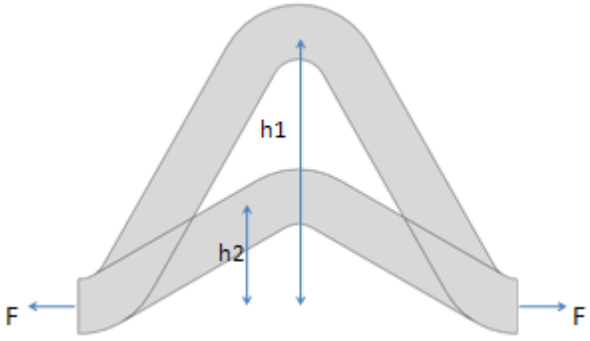

Figure 3.21: Schematics of the force and moment arm for different h corrugations.

H	Direct read force	Calculated force by moment theory*	Error%
2	47.58	42.7	11.42
3	30.33	28.47	6.54
4	21.72	21.35	1.73
5	17.08	-	-

Table 3.1: Comparison between direct read forces and calculated forces.

$$M = F \times h \tag{3-1}$$

$$F_2 = \frac{F_1 \times h_1}{h_2} \tag{3-2}$$

The second column in Table 3.1 is the directly read force at the bottom bend. To recall in Figure 3.20, the S11 stress distribution for high h value overlaps while it differs noticeably for small h case. Therefore, the force obtained from simulation for h=5 case is used in Equation (3-2) to calculate the force for h=4, 3, 2 cases. The third column records the calculated forces. The calculated forces for h=4 and h=3 cases match the directly read results. The results for h=2 case, however, show some discrepancy, which is caused by the influence of the thickness and bend radius as mentioned earlier.

The h/p ratio determines the necking strain, and h alone governs the strength. Keeping this in mind, reducing both h and p while the ratio of the two is kept constant will produce high necking strain corrugation with high strength. A large scale corrugation is compared with series of four small scale corrugations with the same initial length as shown in Figure 3.22. Both cases have the same h/p ratio of 0.375 and the same initial length of 16. The amplitude for large scale case h1 is 6, and the amplitude for small scale case h2 is 1.5. The area of the large scale case is 20.197 while the area of the series of small scale is 21.3. Due to the geometry constraint, two areas differ by 5%. Although the same amount of material in both cases is preferred, the two cases are still comparable.

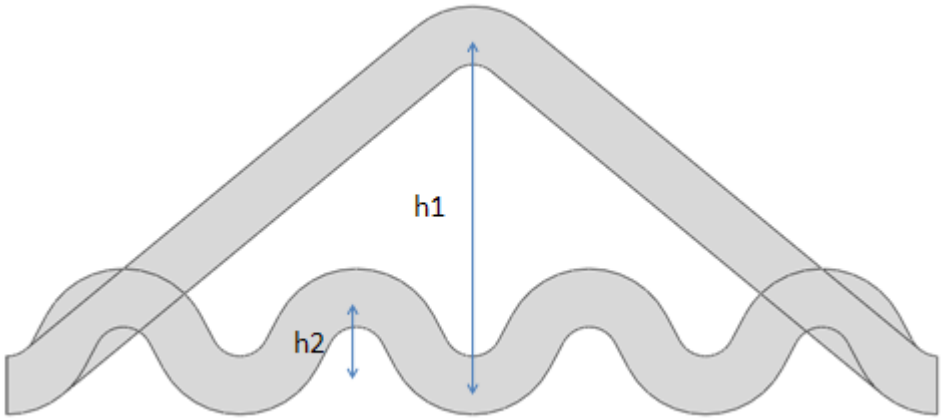

Figure 3.22: Schematics of corrugations with different scale.

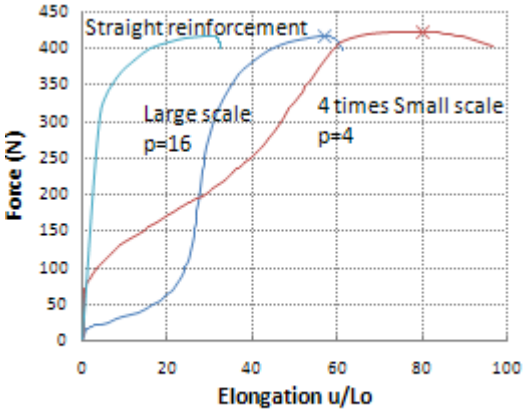

Figure 3.23: Tensile behavior for corrugations with different scales.

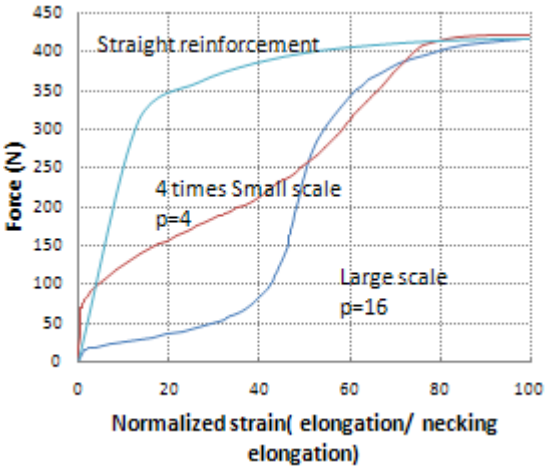

Figure 3.24: Tensile behavior with normalized strain for corrugations with different scales.

The straight specimen is added for comparison. As shown in Figure 3.23, the straight case necks at 30.8% elongation, and the large scale case necks at 56.9%. The series of small corrugation case has the highest necking strain of 79.9%. In Figure 3.24, all three cases have the similar maximum force before necking with difference of only 1.3%. It is clearly shown that the series of small corrugation specimens exerted much higher force from the beginning up to 50% of the normalized strain than the large scale case. After 50% normalized strain, the two force curves both have increasing trend to the maximum value and similar magnitude because the corrugations are stretched and the material properties take effect. For the same thickness, same h/p value and same amount of material, reinforcement with series of small corrugation is superior to the reinforcement consisting of one large corrugation in both necking strain and strength.

The optimal case is always in the ultimate interest. According to the above results, reinforcement consisting of series of small corrugations is better compared to the reinforcement with one large corrugation, but how small is the optimal? If the corrugation scale is reduced to really small, the corrugations become the surface roughness and the reinforcement is straight again. Therefore, there must be a corrugation scale limit for the best corrugated reinforcement.

The optimal corrugation scale is studied by continuing reducing the period of the corrugation while the h/p value and thickness are kept unchanged. This scale effect can be seen as the thickness effect. Reducing the corrugation scale while keeping the thickness constant is the same as keeping the scale same and increasing the thickness. However, taking the number of corrugations N within a specific length as the scale indicator is more vivid and continuous from the previous results than the thickness. Due to the constraint of the bend radius, the maximum number of corrugations N in the 16 mm long reinforcement is limited to 8. Triangular corrugation has no geometric constraint, and the number of corrugations N can reach infinite. Therefore, triangular corrugations with thickness of 0.8 mm are used for the optimal scale study as shown in Figure 3.25. The corrugation thickness is changed to 0.8 mm in triangular case, so the thickness at the bend is kept to 1mm, which is the same as in previous arc-straight cases.

Figure 3.25: Schematics of the triangular corrugation used in determining the optimal scale.

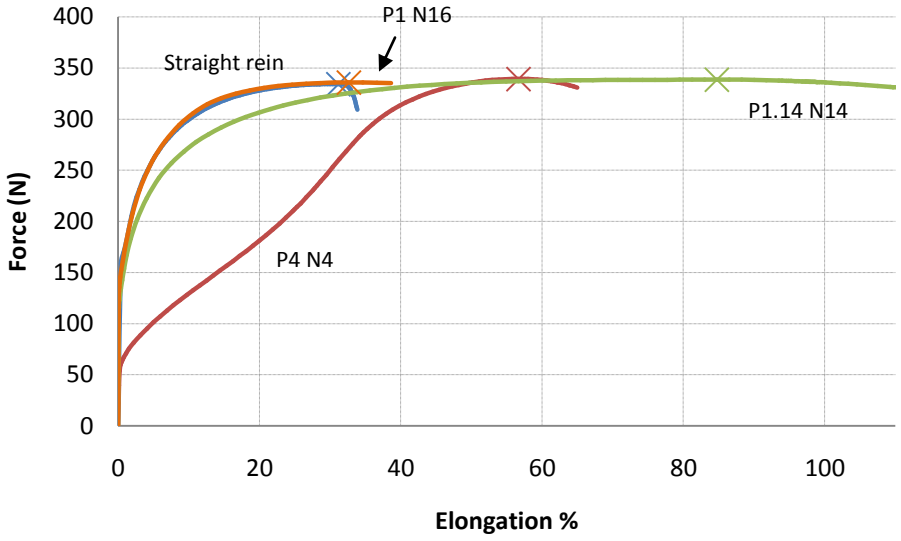

Figure 3.26: Tensile behavior comparison for triangular different N cases.

Figure 3.26 is the force versus elongation percentage plot of the different N cases for triangular corrugations. The N, number of corrugations in 16mm reinforcement, is increased from 4 to 16. The maximum force for all the cases including straight case are the same while the force at initial stage increases as the increase of N. In Figure 3.27, the necking strain increases as the N increases, and it reaches the peak of 84.7% at N=14. As the N continues to increase to 16, the necking strain drops to 32.6%, which is close to the straight case of 30.8%. For the thickness of 0.8mm, h/p=0.375, length of 16mm

corrugated reinforcement, N=14 or p=1.14 mm is the optimal configuration, having the highest necking strain of 84.7% and considerable high strength.

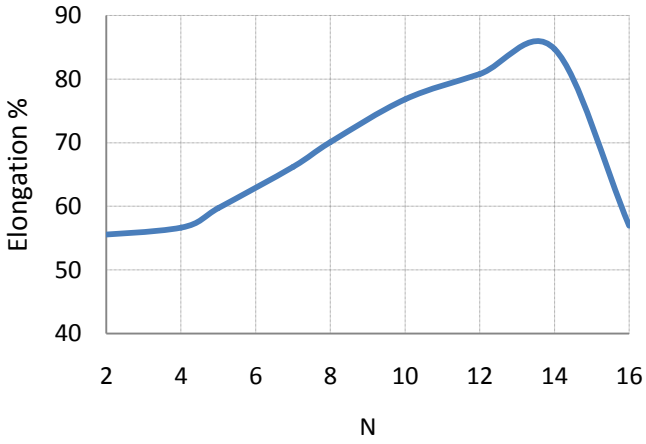

Figure 3.27: N effect on necking strain.

3-3 Effect of corrugated reinforcement in composite material

The ultimate goal for corrugated reinforcement is to improve the necking strain and strength of the composite sheet metal. The optimal configuration of the reinforcement has been produced above. The reinforcement is combined with the matrix material to form the composite, and the effect of the corrugated reinforcement on the composite material is studied. The composite sheet metal is assumed to have infinite width and thickness of 3.5 mm. The matrix material has 210 GPa Young's modulus, 0.3 Poisson's ratio, 43 MPa yield stress, 183 MPa strength coefficient and 0.204 hardening index, and the reinforcement material has the same Young's modulus and Poisson's ratio, 163 MPa yield stress, 650 MPa strength coefficient and 0.27 hardening index. The reinforcement is

a stronger and more ductile material than the matrix. To be comparable with the reinforcement only results, the h/p value is fixed to 0.375, and the thickness for triangular and the arc-straight reinforcement are 0.8 mm and 1 mm respectively. The structures of the composite are shown in Figure 3.28. Due to the 3.5mm thickness of the composite and the fixed h/p value, the maximum permitted period is 6.67 mm. For this case, the corrugation scale is N=2.4. The N is the number of corrugations in 16 mm length as prescribed above. The volume fraction for triangular reinforcement cases are all 28.57%, and 36.71% for all arc-straight reinforced composites. The scale is then reduced to N=4 and N=6. The geometry enables the scale to be further reduced to N=14 for triangular case.

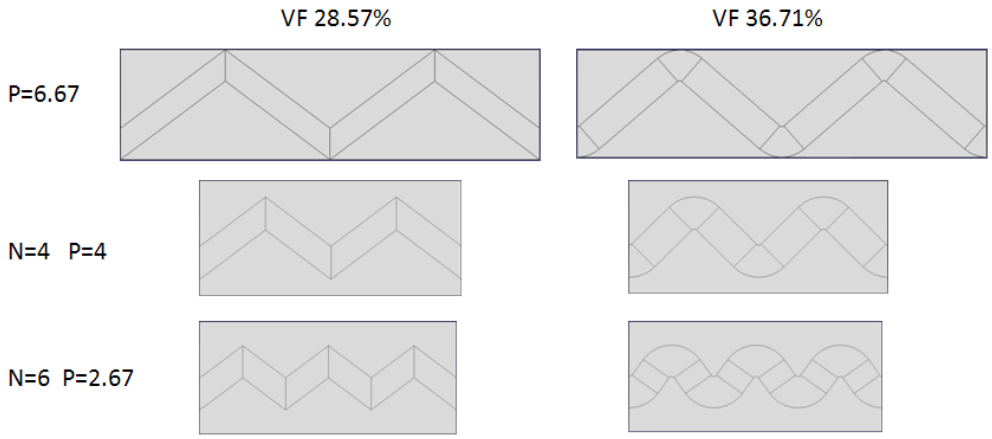

Figure 3.28: Schematics of composite: (a) with triangular reinforcement, and (b) with arc-straight reinforcement.

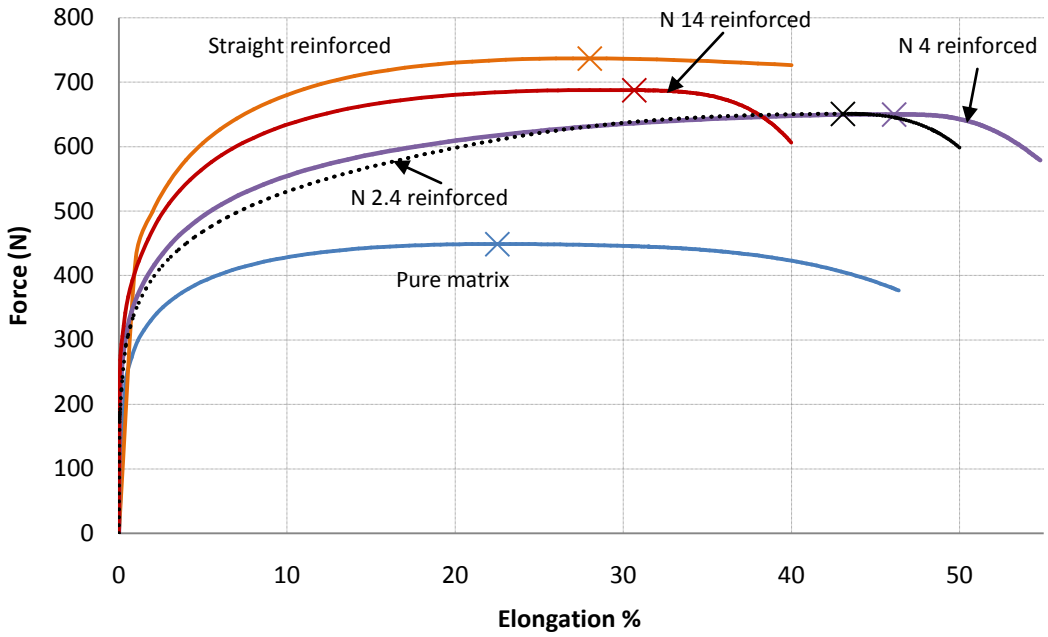

Figure 3.29: Tensile behavior comparison for composite with different scale triangular reinforcement.

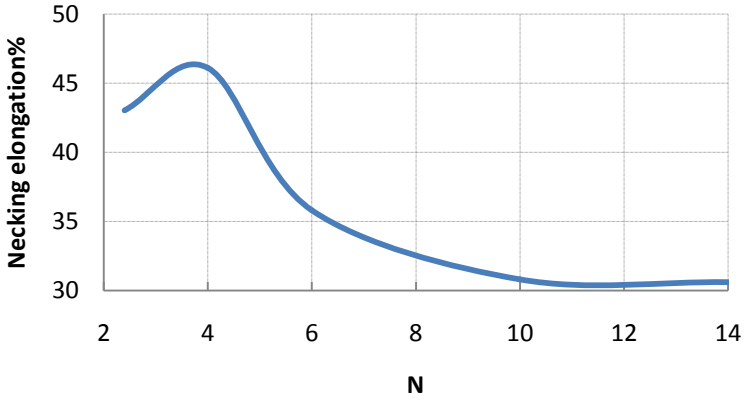

Figure 3.30: Scale effect on the necking strain for composite with triangular reinforcement.

Figure3.29 is the force versus elongation % for composites with different triangular reinforcement. The pure matrix case has the maximum force of 448 N, and it necks at 22.5% strain. The straight reinforcement significantly improved both the

maximum force and necking strain to 736 N and 28%, respectively. The triangular corrugation reinforced composite has slightly lower strength and well improved necking strain. In Figure 3.30, as the N decreases from 14 to 2.4, the necking strain increases. It peaks at 46.1% for N=4 case. Further reduction of the N results in the drop of necking strain. The maximum force for corrugation reinforced composites are very close around 650 N except the N=14 case, whose behavior is close to the straight reinforced case. The N=4, p=4 triangular reinforced case is the optimal case since it has the highest necking strain and considerably high strength. Comparing N=14, which is the optimal case for reinforcement only, the best reinforcement geometry doesn't yield the best composite structure, and the complex interaction between the reinforcement and the matrix should be the reason. Both reinforcement geometry and the difference between the material properties of the reinforcement and the matrix will affect the optimal structure for the composite.

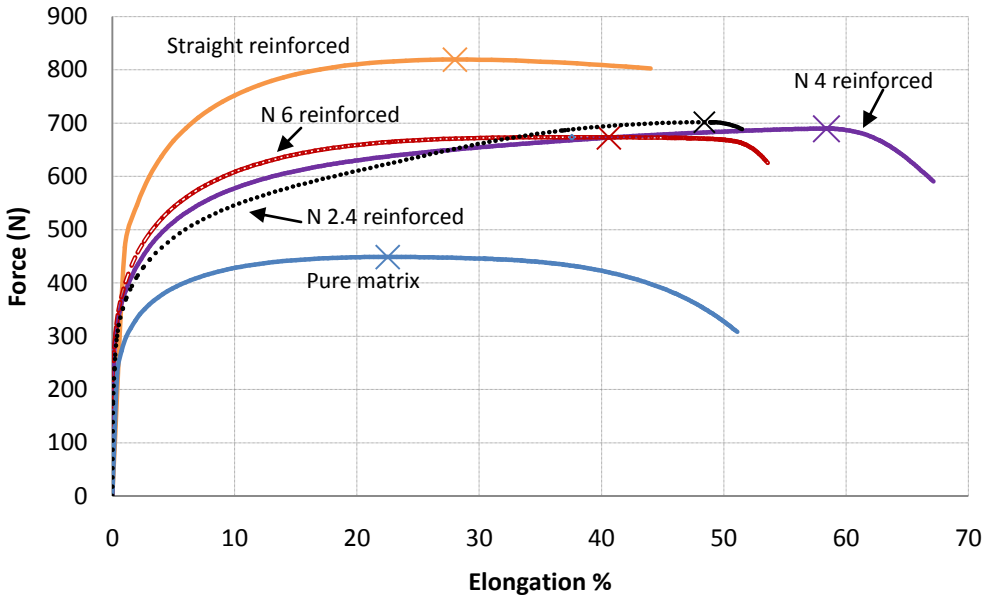

(a)

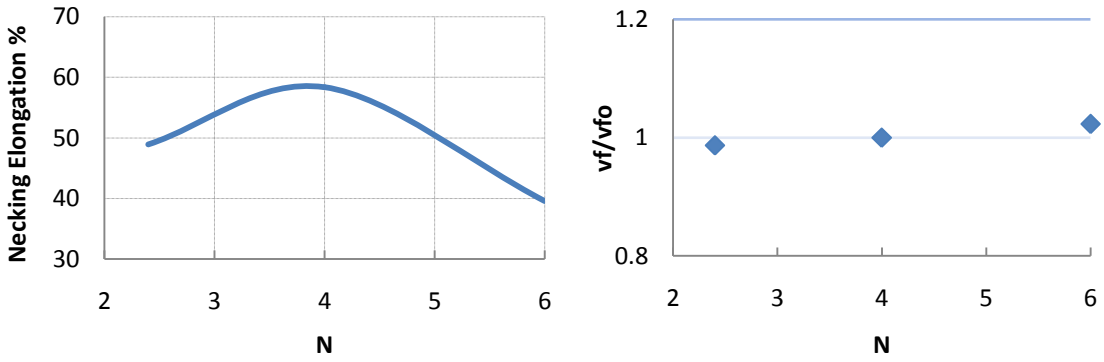

(b) (c)

Figure 3.31: (a) Tensile behavior comparison for arc straight reinforced composite with different scale, (b) Scale effect on necking strain when VF.=36.71%, and (c) Volume fraction variation for different scale.

Figure 3.31(a) is the force versus percent elongation for composites with arc-straight reinforcement. Due to the higher reinforcement volume fraction compared with the triangular reinforced cases, the maximum forces for corrugated reinforced composites

are around 700 N. The N is increased from 2.4 to 6. The necking strain increases as the N is increased. It reaches the peak value of 58.37% for N=4 case. Additional increase of N results in decreasing of necking strain as shown in Figure 3.31(b). N=4, p=4 produced the optimal structure for arc-straight corrugation reinforced composite because of the highest necking strain and considerably high strength. The arc bend causes the variation of the volume fraction of the reinforcement as shown in Figure 3.31(c). However, the differences are within 2%, so the results are comparable.

3-4 Conclusion

In this chapter, series of finite element analysis about uniaxial tensile test of corrugated reinforcement and its composites have been conducted. The ultimate goal is to produce a composite material having high necking strain and high strength although the two properties are usually contradictory. At the beginning, corrugations made by two different methods are compared. Due to the lost of strain hardening during the pressing process, pressed corrugation necks earlier than the cast ones although the pressed corrugation shows some improvement of necking strain compared to the straight case. Cast corrugation is preferred in subsequent studies. Parameters portraying a corrugation have been detailed studied to yield the optimal independent corrugated reinforcement. The h/p value, the ratio between the amplitude and the period, has significant impact on tensile behavior of the reinforcement. A high h/p value indicates high necking strain but

low strength and vice versa. However, the h/p ratio alone cannot produce the optimal configuration, so it should be chosen according to applications. The shape and bend radius has little effect on the tensile behavior. With the same h/p value and thickness, small scale corrugations are superior to large scale corrugations in both necking strain and strength. There is an optimal scale for independent corrugations to produce the highest necking strain and strength. Further decrease of the scale would result in dropping of uniform tensile strain. Strong and ductile corrugated reinforcement can improve both strength and necking strain of the matrix material. There is an optimal structure for the composite with corrugated reinforcement. However, this reinforcement configuration is different from the optimal configuration for the independent corrugated reinforcement.

Chapter 4 Strain hardening and formability improvement of 3D cone reinforced composite.

4-1 Introduction

It is well known that formability is proportional to the strain hardening rate. In the previous chapter, 2D finite element models proved that corrugated reinforcement can significantly increase composite strain hardening and necking strain. However, the improved necking strain is only along the tensile direction. In other words, the simple 2D corrugation cannot be beneficial to the necking strain in in-plane direction. In the sheet metal industry, this anisotropy may result in failure in in-plane direction, so the application of the 2D corrugation reinforced composite is limited. In this chapter, the 2D corrugation is developed to three dimensional, so the strain hardening rate and necking strain in both directions can be increased, and the formability of the composite can be improved. Usually the formability is represented by forming limit diagram FLD. The FLD records the major strain and minor strain associated with the failure in different strain path stretching as demonstrated in Figure 4.1. The strain ratio ranges from -5 to 0 and to 1. At strain ratio of -5, the sheet is under uniaxial tension. The sheet experiences in-plane plane strain tension when the strain ratio is zero while it experiences equal biaxial stretch when the strain ratio is 1. The in-plane plane strain path is critical since the sheet fails at smallest strain comparing with other strain paths, indicating the sheet will most likely fail under this condition. Therefore, this chapter will focus on the effect of 3D corrugation on formability under in-plane plane strain conditions.

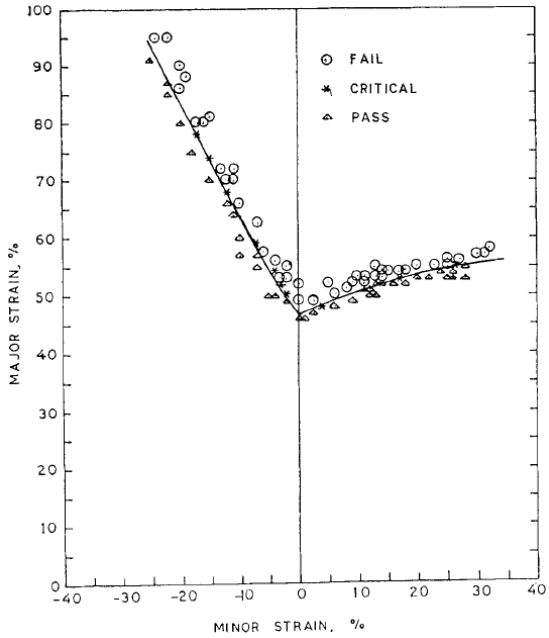

Figure 4.1: Forming limit diagram for EDD steel. [Paul et al. (1996)]

4-2. Modeling and results

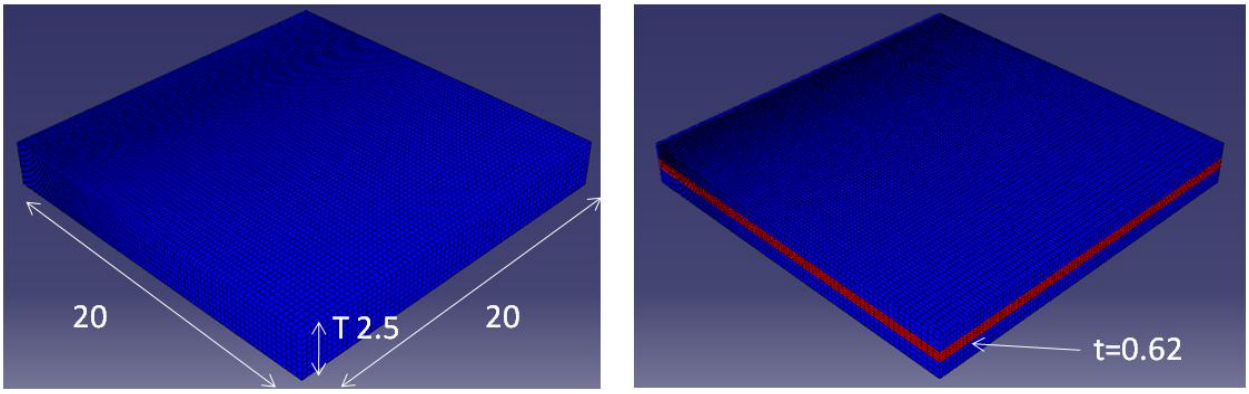

(a) (b)

Figure 4.2: Schematics of the base models. (a) Dimensions of the specimen, and (b) Dimension of the flat reinforcement.

The materials used have power hardening behavior. The matrix have Young's modulus of 70 GPa, Poisson's ratio v=0.3, yield stress 43 MPa, strength coefficient K=183 MPa and hardening index n=0.204. The reinforcement have the same elastic modulus and Poisson's ratio, while the yield stress is 110 MPa, K=500 MPa and n=0.3. The specimen is 20 in length, 20 in width and 2.5 in thickness as illustrated in Figure 4.2. This dimension is chosen to ensure the adequate aspect ratio of 8. Pure matrix case and flat reinforced case are used to compare the stretching behavior with the corrugated case. The two benchmark cases need imperfections to trigger the instability. The imperfection is induced by the cosine wave equation $\Delta = A \times \cos(\frac{x}{20}\pi)$. The amplitude A is 0.5% of the thickness. For the flat reinforced case, the volume fraction of the reinforcement sheet is 24.7%, and this volume fraction will be used in the subsequent analysis.

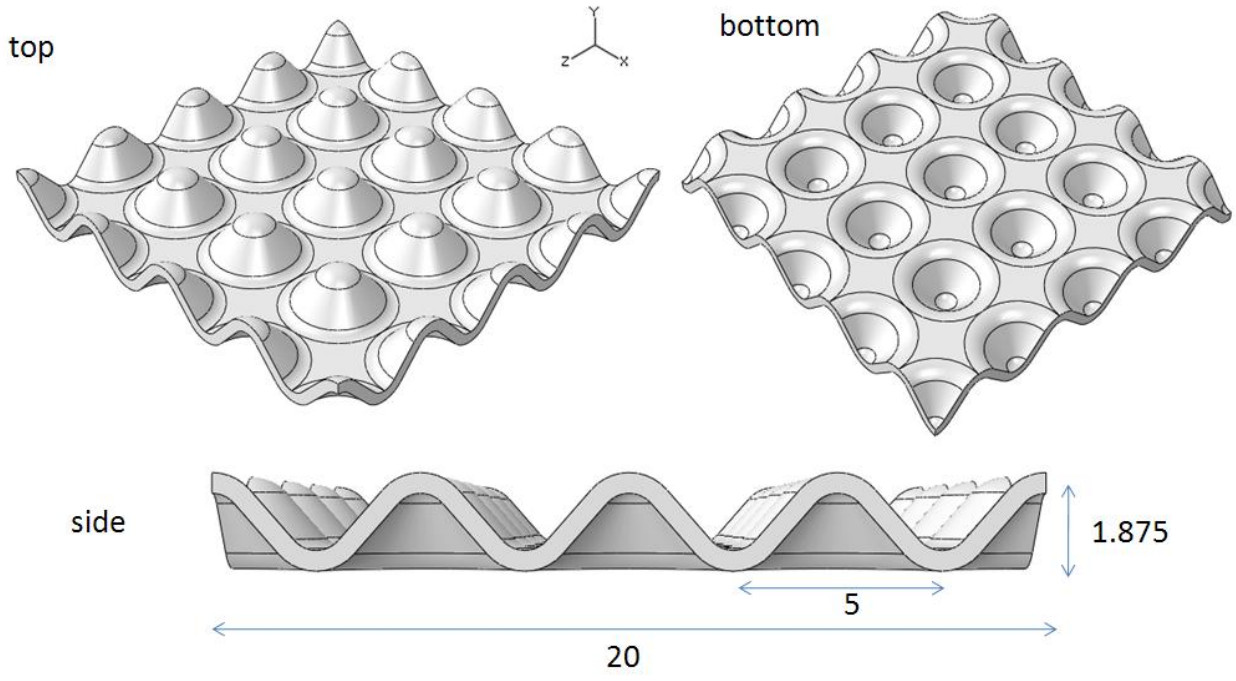

Figure 4.3: Schematics of the cone reinforcement.

The cone reinforcement is schematically shown in Figure 4.3. The side profile can be seen as a series of corrugations. The amplitude is 1.875 which is the height of the cone. The period is 5 which is the base diameter of the cone. The h/p ratio is 0.375. The thickness of the reinforcement is 0.5. The cones are directly connected to each other along the orthogonal directions while there are some flat blanks between the cones along diagonal directions. The sides perpendicular to the z axis of the specimen are constrained to induce plane strain condition while one side perpendicular to the x axis is stretched and the other is constrained along x direction.

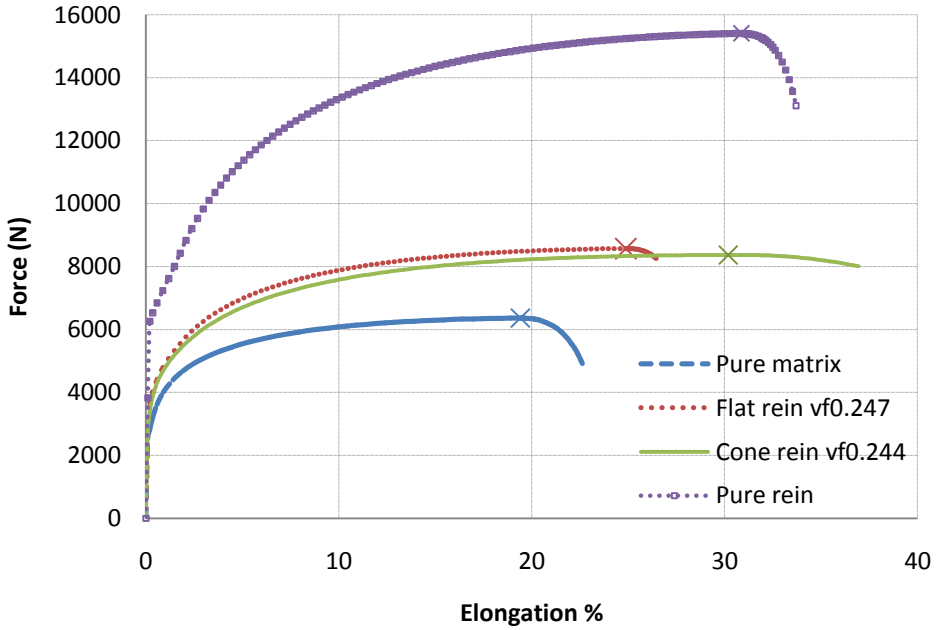

Figure 4.4: Plane strain tensile behavior comparison.

Pure matrix material case, pure reinforcement material case, flat reinforced case and cone reinforced case are stretched, and the tensile behaviors for the four cases are compared in Figure 4.4. Due to the nature of the material properties, the maximum force

for pure matrix material case is 6362 N, and the necking strain is 19.41%. Both the maximum force and necking strain are the lowest among the four cases. In contrary, the pure reinforcement material case has the highest maximum force of 15409 N and necking strain of 30.81%. The flat reinforced case has moderate maximum force of 8571 N and necking strain of 24.87%. The maximum force for cone reinforced case is similar as the flat reinforced case, and it reaches 8366 N. The necking strain for the cone reinforced case is significantly improved to 30.19%, which is very close to the pure reinforced material case. The necking strain is improved by 55.5% comparing with pure matrix material case, and by 21.4% even comparing with flat reinforced case. In other words, replacing 24.7% of the specimen volume by cone reinforcement, the composite has very similar necking strain as if pure reinforcement material is used. In addition, the maximum force is improved by 31.5% compared to the pure matrix material case. Clearly, the cone reinforcement significantly improved the formability and load carrying ability, and it is superior to the flat reinforcement.

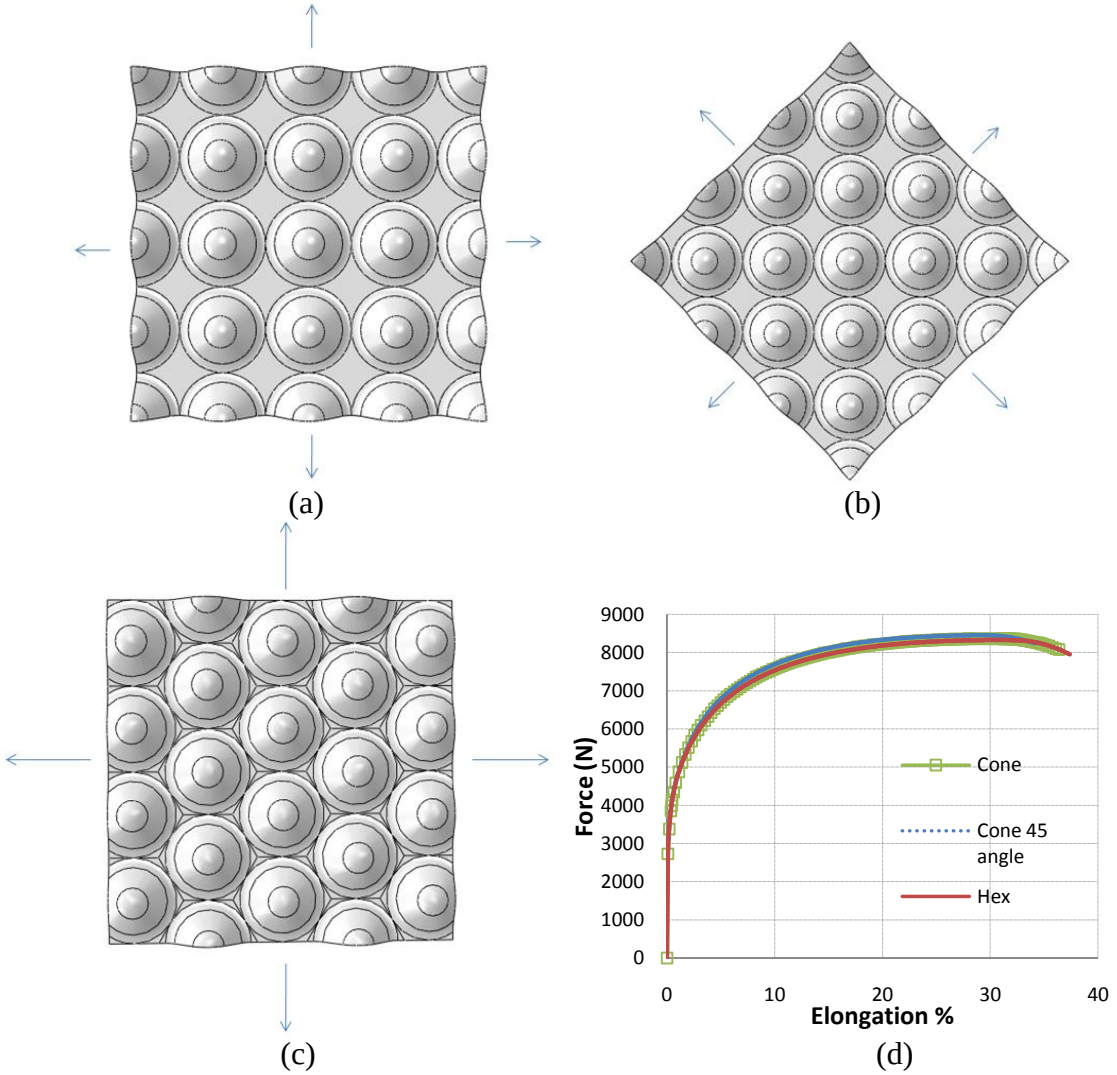

Figure 4.5: Different arrangement of cones. (a) Quadrilateral arrangement; (b) 45 degree arrangement; (c) Hexagonal arrangement; (d) Tensile behaviors for different cone arrangement.

In sheet metal industry, due to the anisotropy of the sheet metal, usually the tensile behavior for rolling direction, transverse direction and 45 degree direction are different. Similarly, the behavior of the cone reinforced composite may vary according to different cone arrangement. Figure 4.5(a) shows the quadrilateral arrangement which is used in the previous comparison in Figure 4.4. Figure 4.5(b) is the 45 degree arrangement.

In this case, the cones directly connect with each other along diagonal directions with respect to the tensile direction, and the flat part is between the cones in the tensile direction. In all polygons, only quadrilateral and hexagon can make a surface by repeating itself. Figure 4.5(c) is the hexagonal arrangement. The cones directly touch with each other along the $+30^{o}$ and -30^{o} with respect to the tensile direction. The flat parts between the cones are much smaller comparing with the ones in quadrilateral arrangement. The tensile behaviors of the three cases are compared in Figure 4.5 (d). Due to the different geometry, the length and width are not precisely equal to 20 for hexagonal and 45 degree arrangement. The forces are normalized by dividing its own length of the side and then times 20. The three curves are very close and almost overlap. The 45 degree case has the highest maximum force of 8452 N and lowest necking strain of 29% while the hexagonal case has the lowest maximum force of 8327 N and highest necking strain of 30.8%. For the quadrilateral case, the maximum force and necking strain are 8366 N and 30.2% respectively, which are in between the 45 angle case and hexagonal case.

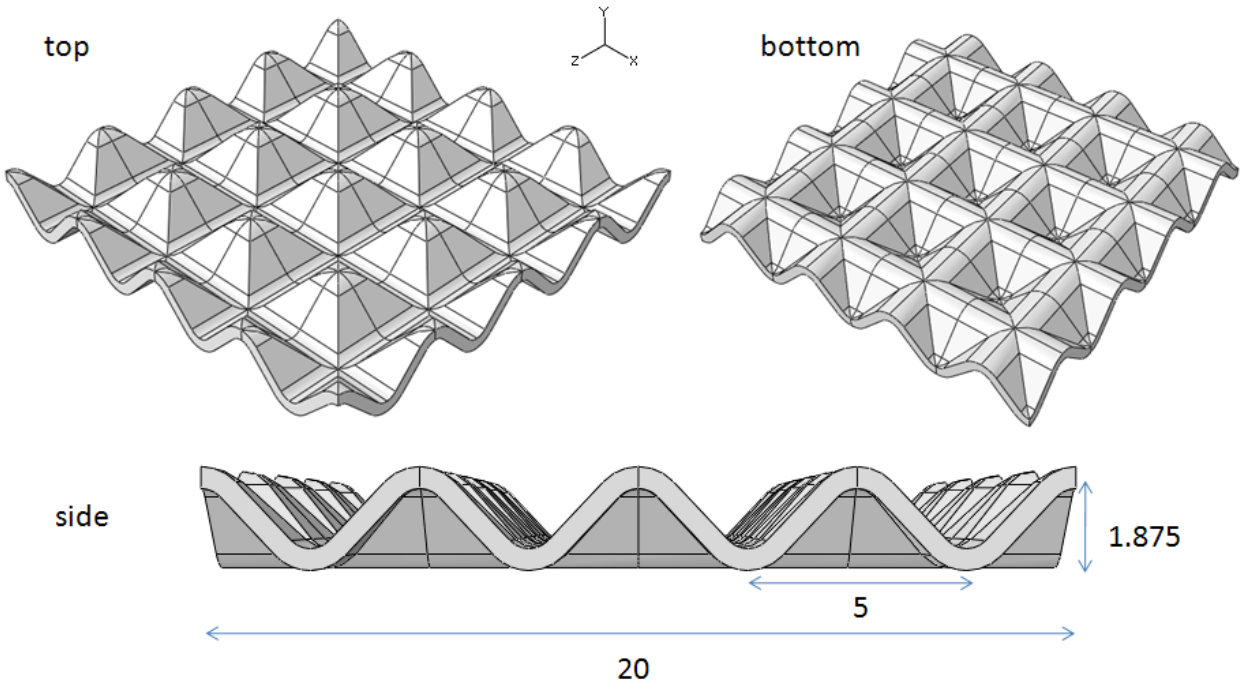

Figure 4.6: Schematics of pyramid reinforcement.

Keeping the side profile as series of corrugation, the reinforcement can be developed to different shapes. Instead of sweeping the corrugation to make cones, pyramid shape can be created by extruding the corrugation curve along x and z directions as shown in Figure 4.6. The pyramid has the same amplitude and period as cones, and the h/p value is remained to 0.375.

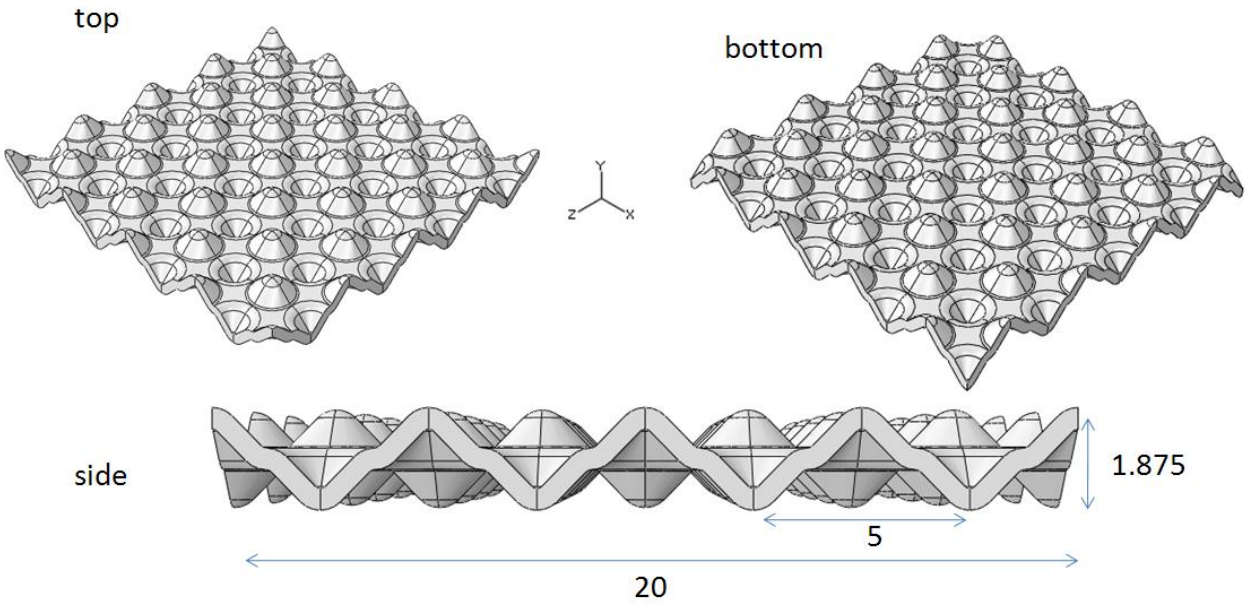

Figure 4.7: Schematics of middle flange cone corrugation.

In both cone and pyramid reinforcement, the cones or the pyramids are connected at the base by flat sheet. The reinforcement can be made by pressing a sheet metal from the bottom using the associated mold. Another type of reinforcement can be made by pressing a sheet from the bottom and the top simultaneously. As shown in Figure 4.7, the cones are connected by a flange at the middle of the height. The corrugation consisted by the top and bottom cones still has the same amplitude and period as in the cone case, and h/p value is 0.375 as well.

The tensile behavior is compared between the cone, pyramid and middle flanged cone cases in Figure 4.8. The curves are very close. The pyramid necks at 30.95% and exerts 8423 N while the middle flanged case necks at 29.5% and exerts 8452 N force. The shape has little effect on tensile behavior.

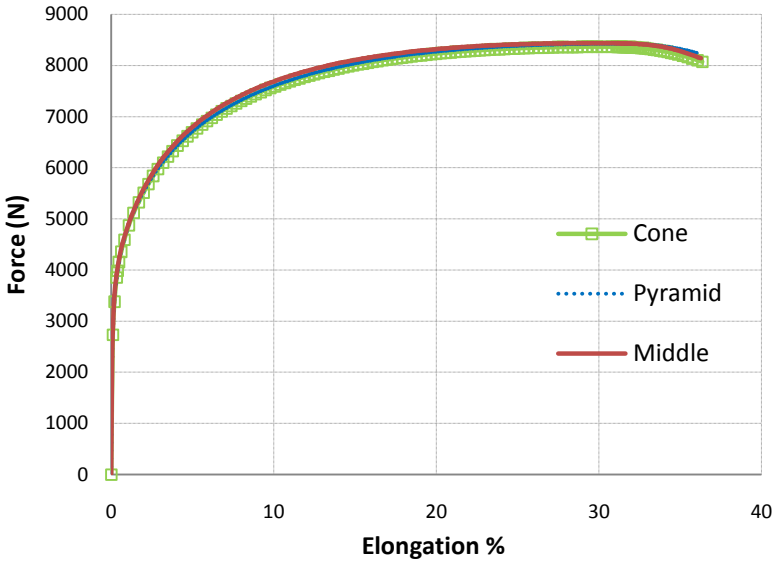

Figure 4.8: Tensile behavior of different shape.

4-3. Conclusion and recommendation

Under in-plane plane strain condition, with 24.7% volume fraction of cone reinforcement, the necking strain of the composite is increased from 19.41% for the pure matrix material case to 30.19% of elongation, which is 55.5% improvement. The load carrying ability is increased from 6361 N to 8366 N, which is 31.5% of improvement. The improvement of necking caused by cone reinforcement is superior to it caused by flat reinforcement while the strengths of the cases are similar.

Different arrangement of the cones and different shapes of the reinforcement exist, but they have little effect on the tensile behavior of the composite.

Much additional research can be done based on the present results. The effect of the parameters such as amplitude, period or h/p ratio and scale factor on necking strain and force can be evaluated as in 2D corrugation reinforced composite. The sheet can be stretched along different strain paths, and a complete FLD can be generated.

Chapter 5 Conclusions

Adding high strain hardening clad material increases the overall strain hardening rate and necking strain of the composite. The relations between the clad thickness ratio and the necking strain and clad material strain hardening index and the necking strain are not linear. Equation (2-1-7) can be a good prediction of necking strain for laminated composite.

After the unloading in pure bending process, the shrinkages at the outer surface and the center are different, and this difference causes compressive and tensile S11 residual stress at the top and bottom respectively for monolithic specimen and soft outer layer composite. Other residual stress distribution exits according to different material composition. As the bending increases, the neutral axis is shifted downward. Material composition affects the rate and value of the move of the neutral axis. The curvature change in springback is linearly related to the bending moment while the Young's modulus, Poisson's ratio and moment inertia determine the slope of the linear relation.

Tensile and compressive S11 residual stresses are distributed at the top and bottom surfaces after unloading for the hydroforming process. More compressive residual stress at the outer layer is observed when soft material is cladded. The volume change of the specimen is linearly related to the fluid pressure while the slope of the linear relation is independent to the material composition.

In 2D plane strain tension, corrugated reinforcement can significantly improve necking strain of the composite due to the strain hardening rate at large strain provided by the corrugations. Results show that the necking stain improvement induced by corrugated reinforcement surpasses improvement induced by straight reinforcement. A high h/p value is associated with high necking strain but low strength while shape has little effect on the tensile behavior. Small scale corrugation is superior to large scale ones. However, an optimal scale exists for highest necking strain and considerable strength. Further decrease of the scale deteriorates the necking strain.

As the 2D corrugated reinforcement is developed to 3D cone reinforcement, the necking strain improvement in one direction is broadened to other directions. Under plane strain condition, the necking strain of cone reinforced composite is superior to the necking strain of flat reinforced composite while the strength of the two cases are comparable.

Bibliography

ABAQUS Analysis User's Manual, Version 6.5, 2005. ABAQUS Inc., Providence, Rhode Island, USA.

Ahmed, S.F.U., & Maalej, M. (2009). Tensile strain hardening behavior of hybrid steel-polyethylene fiber reinforced cementitious composites. Construction and Building Materials, 23, 96-106.

Alexandrov, S., & Hwang, Y.M. (2009). The bending moment and springback in pure bending of anisotropic sheets. International Journal of Solids and Structures, 46, 4361-4368.

Ali, W.J., & Balod, A.O. (2006). Theoretical determination of forming limit diagram for steel, brass and aluminum alloy sheets. Al-Rafidain Engineering Journal, 15, 40-55.

Ashby, M.F., & Brechet, Y.J.M. (2003). Designing hybrid materials. Acta Materialia, 51, 5801-5821.

Ayyar, A., & Chawla, N. (2006). Microstructure-based modeling of crack growth in particle reinforced composites. Composites Science and Technology, 66, 1980-1994.

Bouaziz, O., Allain, S., Barcelo, D., & Niang, R. (2009). Strengthening by plastic corrugated reinforcements: An efficient way for strain-hardening improvement by architecture. Materials Research Society Symposium Proceedings, 1188, 111-115.

Bouaziz, O., Allain, S., & Scott, C. (2008). Effect of grain and twin boundaries on the hardening mechanisms of twinning-induced plasticity steels. Scripta Materialia, 58, 484-487.

Bouaziz, O., Brechet, Y., & Embury, J.D. (2008). Heterogeneous and architectured materials: A possible strategy for design of structural materials. Advanced Engineering Materials, 10, 24-36.

Bouaziz, O., & Guelton, N. (2001). Modelling of TWIP effect on work-hardening. Materials Science and Engineering, A319-321, 246-249.

Bouwhuis, B.A., Chehab, B., Bouaziz, O., Embury, J.D., Zurob, H., & Hibbard, G.D. (2010). Deformation twinning as a strengthening mechanism in microtruss cellular materials. Scripta Materialia, 63, 609-612.

Bruni, C., Celeghini, M., Geiger, M., & Gabrielli, F. (2007). A study of techniques in the evaluation of springback and residual stress in hydroforming. The International Journal of Advanced Manufacturing Technology, 33, 929-939.

Chehab, B. Zurob, H. Embury, J.D., Bouaziz, O., & Brechet, Y. (2009). Compositionally graded steels: A strategy for materials development. Advanced Engineering Materials, 11, 992-999.

Chen, W.H. (1971). Necking of a bar. International Journal of Solids and Structures, 7, 685-717.

Chen, Z.T., Worswick, M.J., Pilkey, A.K., & Lloyd, D.J. (2005). Damage percolation during stretch flange forming of aluminum alloy sheet. Journal of the Mechanics and Physics of Solids, 53, 2692-2717.

Chen, X.X., Wu, P.D., Embury, J.D., & Huang, Y. (2010). Enhanced ductility in round tensile bars produced by cladding a ductile ring. Modelling and Simulation in Materials Science and Engineering, 18, 025005-1 - 025005-18.

Chen, X.X., Wu, P.D., Lloyd, D.J., Embury, J.D., Huang, Y. (2010). Enhanced ductility in sheet metals produced by cladding a ductile layer. Journal of Applied Mechanics, 77, 041015-1 - 041015-7.

Chien, W.Y., Pan, J., & Tang, S.C. (2004). A combined necking and shear localization analysis for aluminum sheets under biaxial stretching conditions. International Journal of Plasticity, 20, 1953-1981.

Dan, W.J., Li, S.H., Zhang, W.G., & Lin, Z.Q. (2008). The effect of strain-induced martensitic transformation on mechanical properties of TRIP steel. Materials and Design, 29, 604-612.

El-Megharbel, A., El-Domiaty, A., & Shaker, M. (1990). Springback and residual stresses after stretch bending of work hardening sheet metal. Journal of Materials Processing Technology, 24, 191-200.

Embury, J.D., & Bouaziz, O. (2010). Steel- based Composites: Driving forces and classifications. Annual Review of Materials Research, 40, 213-241.

Ganser, H.P., Werner, E.A., & Fischer, F.D. (2000). Forming limit diagrams: a micromechanical approach. International Journal of Mechanical Sciences, 42, 2041-2054.

Gau, J.T., & Kinzel, G.L. (2001). A new model for springback prediction in which the Bauschinger effect is considered. International Journal of Mechanical Sciences, 43, 1813-1832.

Guild, F.J., & Summerscales, J. (1993). Microstructural image analysis applied to fiber composite materials: a review. Composites, 24, 383-393.

Hutchinson, J.W., & Miles, J.P. (1974). Bifurcation analysis of the onset of necking in an elastic/plastic cylinder under uniaxial tension. Journal of the Mechanics and Physics of Solids, 22, 61-71.

Inal, K., Simha, H.M., & Mishra, R.K. (2008). Numerical modeling of second-phase particle effects on localized deformation. Journal of Engineering Materials and Technology, 130, 021003-1 - 021003-8.

Jacques, P., Furnemont, Q., Pardoen, T., & Delannay, F. (2001). On the role of martensitic transformation on damage and cracking resistance in TRIP-assisted multiphase steels. Acta Materialia, 49, 139-152.

Kang, D.H., Kim, D.W., Kim, S., Bae, G.T., Kim, K.H., & Kim, N.J. (2009). Relationship between stretch formability and work-hardening capacity of twin-roll cast Mg alloys at room temperature. Scripta Materialia, 61, 768-771.

Kleiner, M., Krux, R., & Homberg, W. (2004). Analysis of residual stresses in high-pressure sheet metal forming. CIRP Annals-Manufacturing Technology, 53, 211-214.

Ko, Y.G., Lee, C.W., Namgung, S., & Shin, D.H. (2010). Strain hardening behavior of nano-structured dual-phase steel processed by severe plastic deformation. Journal of Alloys and Compounds, 504s, 452-455.

Lademo, O.G., Pedersen, K.O., Berstad, T., Furu, T., & Hopperstad, O.S. (2008). An experimental and numerical study on the formability of textured AlZnMg alloys. European Journal of Mechanics A/Solids, 27, 116-140.

Lahaie, D.J., Embury, J.D., & Ashby, M.F. (1995). Scale dependent composite design charts. Scripta Metallurgica, 32, 133-138.

Lefevre-Schlick, F., Bouaziz, O., Brechet, Y., & Embury, J.D. (2008). Compositionally graded steels: The effect of partial decarburization on the mechanical properties of spherodite and pearlite. Materials Science and Engineering, A 491, 80-87.

Lievers, W.B., Pilkey, A.K., & Lloyd, D.J. (2003). The influence of iron content on the bendability of AA6111 sheet. Materials Science and Engineering, A 361, 312-320.

Ling, Y. (1996). Uniaxial true stress-strain after necking. AMP Journal of Technology, 5, 37-48.

Mackerle, J. (2002). Metal matrix composites: finite element and boundary element analysis a bibliography (1997-2000). Finite Elements in Analysis and Design, 38, 659-667.

Marciniak, Z., & Kuczynski, K. (1967). Limit strains in the processes of stretch-forming sheet metal. International Journal of Mechanical Sciences, 9, 609-620.

Mirko, C., & Stefano, S. (2003). Transformation induced plasticity, twinning induced plasticity and dual-phase steels. Special Treatise on Materials Science, Department of Material Science, Tampere University of Technology.

Needleman, A. (1972). A numerical study of necking in circular cylindrical bars. Journal of the Mechanics and Physics of Solids, 20, 111-127.

Oliveira, M.C., Alves, J.L., Chaparro, B.M., & Menezes, L.F. (2007). Study on the influence of work-hardening modeling in springback prediction. International Journal of Plasticity, 23, 516-543.

Paul, S.K., & Mishra, S. (1996). On the formability of sheet steels. Bulletin of Material Science, 19, 963-984.

Peng, J., Wu, P.D., Huang, Y., Chen, X.X., Lloyd, D.J., Embury, J.D., & Neale, K.W. (2009). Effects of superimposed hydrostatic pressure on fracture in round bars under tension. International Journal of Solids and Structures, 46, 3741-3749.

Perduijin, A.B., & Hoogenboom, S.M. (1995). The pure bending of sheet. Journal of Materials Processing Technology, 51, 274-295.

Ruys, A., & Sun, D. (2002).Functionally graded materials and their production methods. Retrieved from http://www.azom.com

Segurado, J., Gonzalez, C., & Llorca, J. (2003). A numerical investigation of the effect of particle clustering on the mechanical properties of composites. Acta Materialia, 51, 2355-2369.

Shi, M.F., & Meuleman, D.J. (1995). On certain aspects of strain rate sensitivity of sheet metals. Journal of Materials Engineering and Performance, 4, 321-333.

Shi, Y., Wu, P.D., Lloyd, D.J., & Embury, J.D. (2010). Crystal plasticity based analysis of localized necking in aluminum tube under internal pressure. European Journal of Mechanics A/Solids, 29, 475-483.

Sing, W.M., & Rao, K.P. (1997). Role of strain-hardening laws in the prediction of forming limit curves. Journal of Materials Processing Technology, 63, 105-110.

Song, R., Ponge, D., & Raabe, D. (2005). Improvement of the work hardening rate of ultrafine grained steels through second phase particles. Scripta Materilia, 52, 1075-1080.

Takuda, H., Mori, K., Takakura, N., & Yamaguchi, K. (2000). Finite element analysis of limit strains in biaxial stretching of sheet metals allowing for ductile fracture. International Journal of Mechanical Sciences, 42, 785-798.

Tomita, Y., & Iwamoto, T. (1995). Constitutive modeling of TRIP steel and its application to the improvement of mechanical properties. International Journal of Mechanical Sciences, 37, 1295-1305.

Tvergaard, V. (1993). Necking in tensile bars with rectangular cross-section. Computer Methods in Applied Mechanics and Engineering, 103, 273-290.

Wagstaff, R.B., Lloyd, D.J., & Bischoff, T.F. (2006). Direct chill casting of clad ingot. Materials Science Forum, 519-521, 1809-1814.

Williams, B.W., Oliveira, D.A., Simha, C.H.M., Worswick, M.J., & Mayer, R. (2007). Crashworthiness of straight section hydroformed aluminum tubes. International Journal of Impact Engineering, 34, 1451-1464.

Wu, P.D., Chen, X.X., Lloyd, D.J., & Embury, J.D. (2010). Effects of superimposed hydrostatic pressure on fracture in sheet metals under tension. International Journal of mechanical Sciences, 52, 236-244.

Wu, P.D., Embury, J.D., Lloyd, D.J., Huang, Y., & Neale, K.W. (2009). Effects of superimposed hydrostatic pressure on sheet metal formability. International Journal of Plasticity, 25, 1711-1725.

Wu, P.D., MacEwen, S.R., Lloyd, D.J., & Neale, K.W. (2004). A mesoscopic approach for predicting sheet metal formability. Modelling and Simulation in Materials Science and Engineering, 12, 511-527.

Yan, H.Y. (2008) Strain-hardening behaviors of Trip-assisted steels during plastic deformation. Materials Science and Engineering, A 479, 333-338.

Yoshida, K., Tadano, Y., & Kuroda, M. (2009). Improvement in formability of aluminum alloy sheet by enhancing geometrical hardening. Computational Materials Science, 46, 459-468.

Zhan, M., Yang, H., Huang, L., & Gu, R.J. (2006). Springback analysis of numerical control bending of thin-walled tube using numerical-analytic method. Journal of Materials Processing Technology, 177, 197-201.

Zhang, Z.T., & Hu, S.J. (1998). Stress and residual stress distributions in plane strain bending. International Journal of Mechanical Sciences, 40, 533-543.

Zhu, H.X. (2007). Large deformation pure bending of an elastic plastic power-law-hardening wide plate: Analysis and application. International Journal of Mechanical Sciences, 49, 500-514.